J. Fluid Mech. (1998), *vol.* 358, *pp.* 135–175. Printed in the United Kingdom

Passive scalar statistics in high-Péclet-number grid turbulence

By L. MYDLARSKI AND Z. WARHAFT

Sibley School of Mechanical and Aerospace Engineering Cornell University, Ithaca, NY 14853, USA

(Received 21 March 1997 and in revised form 21 October 1997)

The statistics of a turbulent passive scalar (temperature) and their Reynolds number dependence are studied in decaying grid turbulence for the Taylor-microscale Reynolds number, R_λ, varying from 30 to 731 ($21 \leqslant Pe_\lambda \leqslant 512$). A principal objective is, using a single (and simple) flow, to bridge the gap between the existing passive grid-generated low-Péclet-number laboratory experiments and those done at high Péclet number in the atmosphere and oceans. The turbulence is generated by means of an active grid and the passive temperature fluctuations are generated by a mean transverse temperature gradient, formed at the entrance to the wind tunnel plenum chamber by an array of differentially heated elements. A well-defined inertial–convective scaling range for the scalar with a slope, n_θ, close to the Obukhov–Corrsin value of 5/3, is observed for all Reynolds numbers. This is in sharp contrast with the velocity field, in which a 5/3 slope is only approached at high R_λ. The Obukhov–Corrsin constant, C_θ, is estimated to be 0.45–0.55. Unlike the velocity spectrum, a bump occurs in the spectrum of the scalar at the dissipation scales, with increasing prominence as the Reynolds number is increased. A scaling range for the heat flux cospectrum was also observed, but with a slope around 2, less than the 7/3 expected from scaling theory. Transverse structure functions of temperature exist at the third and fifth orders, and, as for even-order structure functions, the width of their inertial subranges dilates with Reynolds number in a systematic way. As previously shown for shear flows, the existence of these odd-order structure functions is a violation of local isotropy for the scalar differences, as is the existence of non-zero values of the transverse temperature derivative skewness (of order unity) and hyperskewness (of order 100). The ratio of the temperature derivative standard deviation along and normal to the gradient is 1.2 ± 0.1, and is independent of Reynolds number. The refined similarity hypothesis for the passive scalar was found to hold for all R_λ, which was not the case for the velocity field. The intermittency exponent for the scalar, μ_θ, was found to be 0.25 ± 0.05 with a possible weak R_λ dependence, unlike the velocity field, where μ was a strong function of Reynolds number. New, higher-Reynolds-number results for the velocity field, which smoothly follow the trends of Mydlarski & Warhaft (1996), are also presented.

1. Introduction

The objective of this paper is to describe the variation of passive scalar fluctuations, their statistical moments, spectra, structure functions and conditional statistics, as a function of Reynolds number (or Péclet number; see below for definitions) in grid turbulence, the simplest type of turbulent flow that can be generated in the laboratory.

We will pay particular attention to the way the scalar statistics contrast with those of the velocity field in the same flow, the subject of our earlier inquiry (Mydlarski & Warhaft 1996, from here on referred to as M&W). The passive scalar will be temperature and its fluctuations will be produced by a linear mean temperature profile imposed on the air flow.

Using an active grid technique devised by Makita (1991), also described in M&W and §2 of the present work, we have been able to generate turbulent flows up to a Taylor microscale Reynolds number, $R_\lambda (\equiv u\lambda/\nu$ where u is the longitudinal r.m.s. velocity, λ is the Taylor microscale and ν is the kinematic viscosity) of over 700. The R_λ of the atmospheric boundary layer or the ocean surface layer, the sources of the highest Reynolds numbers on this planet, vary from 10^3 to 10^4. So, the results from our wind tunnel experiments are close to the lower end of this range. However, unlike the atmosphere, whose initial conditions are uncontrollable, and in which there exists complex shear, inhomogeneity and statistical non-stationarity making interpretation of results difficult, the wind tunnel flow is stationary, shearless and close to isotropic. Most importantly, in the wind tunnel the Reynolds number can be varied so that trends in statistical properties can be observed. Most turbulence theory predicts behaviour at infinite Reynolds number: only by examining trends at moderate Reynolds number will we have any hope of extrapolating to higher values, and thereby seeing if the results tend to a clear limit. Indeed, only by examining such trends will we be able to address the question of what we mean by 'high-Reynolds-number' and 'high-Péclet-number' turbulence.

Before we turn to the passive scalar field, we will summarize the main findings of M&W who studied the velocity field over the range $50 \leqslant R_\lambda \leqslant 500$ using the active grid. (Subsequently (see §3) we have, by means of a larger grid, extended the range to $R_\lambda \sim 700$.) M&W observed that the velocity field has a marked evolution with Reynolds number. For $R_\lambda < 100$ it exhibits no inertial-subrange intermittency (i.e. $\mu = 0$, see below for definitions) and the scaling region in the spectrum, which is barely apparent, has a slope of around 1.3, much less than the Kolmogorov value of 5/3. We call this *weak turbulence*. By $R_\lambda \sim 200$ there is significant inertial-subrange intermittency associated with a well-developed inertial subrange, which has a slope close to 5/3. The width of this subrange dilates according to the Kolmogorov prediction, i.e. as $R_\lambda^{3/2}$. This is what we call *strong turbulence*. Between $R_\lambda \sim 100$ and $R_\lambda \sim 200$ there is what appears to be a smooth evolution from weak to strong turbulence. Yet our results show that even by $R_\lambda \sim 700$, the intermittency factor is still increasing with Reynolds number and the spectral slope, while close to 5/3, is still significantly less than this (infinite-Reynolds-number) prediction. (It is 1.6 at $R_\lambda \sim 700$.) Extrapolation of our results shows that only by $R_\lambda \sim 10^4$, the high end of atmospheric measurements, will the spectrum slope be indiscernible from 5/3. At this R_λ, our extrapolated results indicate a value of C_1, the Kolmogorov constant (equation (1), below) of 0.5 and a value of μ in the range 0.2 to 0.25. Both these values are consistent with those measured in the atmosphere (Sreenivasan 1995 and Sreenivasan & Kailasnath 1993) and give confidence that the active grid provides a well-conditioned flow field that bridges the gap between previous low-Reynolds-number grid-turbulence experiments (e.g. Comte-Bellot & Corrsin 1966) and those done at high Reynolds number in the atmosphere and oceans (e.g. Boston & Burling 1972). We note that even in the weak turbulence regime, the turbulence is 'fully developed' in the sense that the turbulence dissipation rate ($\epsilon \equiv \nu \langle(\partial u_i/\partial x_j + \partial u_j/\partial x_i)\partial u_j/\partial x_i\rangle$, where repeated indices (over the three orthogonal directions) mean summation; e.g. Hinze 1975) which acts at the small scales can be accurately estimated from the large scales as $\epsilon = Au^3/\ell$, where ℓ

in the integral length scale of the turbulence and A is a constant close to 1. (M&W find its value is 0.9 for this flow.)

The Kolmogorov (1941*a, b*) phenomenology predicts the high-Reynolds-number one-dimensional spectrum for the inertial subrange in the form

$$F_{11}(k_1) = C_1 \epsilon^{2/3} k_1^{-5/3} \tag{1}$$

where $F_{11}(k_1)$ is the one-dimensional streamwise power spectrum of the longitudinal (x-direction) velocity fluctuations, u; k_1 is the longitudinal wavenumber, ϵ is the turbulence energy dissipation rate per unit mass and C_1 is the Kolmogorov constant. Similar definitions (e.g. M&W) may be written for the transverse (y- and z-directions) velocity fluctuations v and w respectively. As we have just mentioned, our active grid turbulence measurements never quite achieve the form of equation (1), although they appear to be asymptoting to it. It is pertinent to ask how the passive scalar spectrum evolves in this light.

In a similar spirit to Kolmogorov, Corrsin (1951) and Obukhov (1949) showed that in the high-Péclet- and Reynolds-number limit, the passive scalar spectrum in the inertial subrange is of the form

$$F_\theta(k_1) = C_\theta \epsilon^{-1/3} \epsilon_\theta k^{-5/3}. \tag{2}$$

Here $F_\theta(k_1)$ is the one-dimensional power spectrum of the scalar fluctuations, θ (temperature fluctuations in the work to follow), ϵ_θ is the average rate at which the scalar variance, $\langle \theta^2 \rangle$, is smeared at the molecular diffusive scale, and C_θ is a constant. As for C_1, it is thought to be universal for high Péclet numbers. The Péclet number Pe_λ is defined here as

$$Pe_\lambda = (v/\kappa) R_\lambda \tag{3}$$

where κ is the thermal diffusivity. For air v/κ (the Prandtl number) is 0.7, so $Pe_\lambda \sim R_\lambda$. We will often use the two parameters interchangeably.

A central postulate of Kolmogorov (1941*a, b*), and of the extensions to the scalar by Obukhov and Corrsin, is that at the dissipation scales, the gradients of the fluctuations (of velocity or the passive scalar) are isotropic. Thus the velocity dissipation rate ϵ may be determined from the streamwise velocity derivative (e.g. Hinze 1975) as

$$\epsilon = 15 v \langle (\partial u/\partial x)^2 \rangle. \tag{4}$$

There is ample evidence (e.g. Saddoughi & Veeravalli 1994; M&W) to suggest that (4) is indeed a very good estimate of ϵ. Note that while the velocity field appears to be locally isotropic for second-order quantities (such as ϵ), this does not constitute a proof of the Kolmogorov hypothesis, which implies isotropy of all of the moments of the derivative p.d.f.

The scalar smearing rate is defined as

$$\epsilon_\theta = 2\kappa \left\langle \left(\frac{\partial \theta}{\partial x}\right)^2 + \left(\frac{\partial \theta}{\partial y}\right)^2 + \left(\frac{\partial \theta}{\partial z}\right)^2 \right\rangle. \tag{5}$$

Isotropy implies that $\epsilon_\theta = 6\kappa \left\langle (\partial\theta/\partial x)^2 \right\rangle$. We will show, however, that even for second-order gradient quantities, the scalar field is not locally isotropic. The departure of the scalar field statistics from conventional Kolmogorov–Obukhov–Corrsin (KOC) phenomenology is a major aspect of the results to be reported here.

Our work has its origins in two earlier experiments done using conventional grids, and extending over the limited range, $30 \leqslant R_\lambda \leqslant 130$. Jayesh, Tong & Warhaft (1994)

investigated the temperature spectrum and compared it with the velocity spectrum, and Tong & Warhaft (1994) studied the statistics of the temperature derivative. Jayesh *et al.* (1994) found that, in marked contrast to the velocity spectrum, the temperature spectrum was consistent with the high-Péclet-number prediction (equation (2)), even at the lowest Péclet numbers measured ($Pe_\lambda \sim 21, R_\lambda \sim 30$). Tong & Warhaft (1994) found that the temperature derivative skewness, $S_{\partial\theta/\partial y} \equiv \langle(\partial\theta/\partial y)^3\rangle/\langle(\partial\theta/\partial y)^2\rangle^{3/2}$, where the derivative, $\partial\theta/\partial y$, is measured along the temperature gradient, was approximately 1.8, and was insensitive to the variation of R_λ (over the limited variation investigated). This violates the notion of isotropy at the small scales (which requires $S_{\partial\theta/\partial y} = 0$), a central postulate of KOC theory. Relating these earlier findings, done at low Reynolds numbers, to those of high-Reynolds-number atmospheric and laboratory shear flow experiments, is the main aim of the present work. In addition to studying spectra and derivative statistics, we will study the conditional statistics so that we can address some of the issues concerning inertial-subrange intermittency, a subject of particular contemporary importance (Nelkin 1994; Frisch 1995; Sreenivasan & Antonia 1997).

2. Apparatus

The experiments were conducted in our two low-speed, low-background-turbulence open-circuit wind tunnels. The vertical wind tunnel is 40.65×40.65 cm^2 in cross-section and 4.5 m long. With the active grid, its maximum R_λ is 473. The work of M&W was carried out in this tunnel. The horizontal wind tunnel is 91.44×91.44 cm^2 in cross-section and 9.1 m long. Here, using an active grid, an R_λ of 731 is achieved. The two tunnels are respectively described, with sketches, in Sirivat & Warhaft (1983) and Yoon & Warhaft (1990).

The active grid design followed that of Makita (1991). It is composed of rotating grid bars to which are attached triangular agitator wings. Stepper motors, located at the end of each grid bar outside the tunnel, rotate the bars. The speed of the grid bar rotation is determined by a square-wave fed to the motor. A square-wave of randomly varying period is also fed to the stepper motor to randomly change its direction of rotation. A detailed description of the grid used in the vertical tunnel, including a sketch and photo, can be found in M&W.

A new scaled-up active grid was built for use in our horizontal tunnel. Its design is almost identical to that of the grid used in the vertical tunnel, but here, the mesh spacing between grid bars, M, is 11.4 cm. This is two and a quarter times that of M&W, so that as for the previous work, the tunnel cross-section is $8M \times 8M$. The larger grid has seven grid bars in the vertical direction and eight grid bars in the horizontal (the outermost horizontal grid bars were now $\frac{1}{2}M$ from the tunnel walls.) Each of the 15 grid bars is a 1.27 cm (outer) diameter aluminium rod with 0.64 mm thick aluminium wings. Every bar is independently driven by a Superior Electric 5 W DC synchronous stepping motor, with 200 steps per revolution. A new stepper motor control now permitted different rotation rates for each bar. Allowing the rotation rate for each bar to vary slightly from a nominal value eliminated the spike in the spectrum of velocity (see M&W, figure 4) which occurred at twice the grid bar rotation frequency. The velocity spectrum will be discussed in §4.

The new active grid was carefully tuned to achieve good cross-stream homogeneity. This was done in the identical manner to that of our previous active grid, namely by attaching 'static wings' to the walls and by drilling holes in the wings near the walls. As in M&W, the grid was operated in two modes. In random mode, the direction

of rotation of the bars changed randomly. The average time between switching was on the order of a rotation period. In synchronous mode, the direction of rotation of each bar did not change and was reversed from bar to bar so as not to add net vorticity to the flow. The initial condition for the grid in the vertical tunnel was set so that all wings on bars oriented in the North-South direction were vertical and all of the East-West wings were horizontal. The horizontal tunnel had the analogous initial condition. The relative orientation of the grid bars in synchronous mode did not change over the measurement period.

The mean cross-stream temperature gradient was produced by a *toaster*, a set of parallel, differentially heated ribbons at the entrance to the settling chamber of the tunnel. Detailed sketches are provided in Sirivat & Warhaft (1983) and Yoon & Warhaft (1990). Once the flow has passed through the screened plenum and contraction, the wakes (of both momentum and temperature) created by the toaster elements are smoothed out. This results in a mean temperature profile in the (almost) laminar region upstream of the grid. The flow then passes through the grid and thermal fluctuations are produced by the turbulence acting against the temperature profile.

In the horizontal tunnel, the direction of the temperature gradient is parallel to the gravitational vector (which we emphasize is not the case in the vertical tunnel). Thus, the presence of a mean temperature gradient allows for the possibility that temperature might not be a passive scalar since the flow field could be affected by the effects of the stratification. This was found not to be the case by comparing the velocity statistics and spectra in the same flow with and without the mean temperature gradient. The standard deviation of the transverse velocity never dropped by more than 4% when the temperature gradient was created, and the spectra did not significantly change. In addition, the ratio of the buoyancy term, $g\langle v\theta\rangle/T_o$, to the dissipation term, ϵ, in the kinetic energy equation, was never greater than 2%. Here, g is the acceleration due to gravity, $\langle v\theta\rangle$ is the kinematic heat flux along the temperature gradient (in the vertical direction for the horizontal tunnel) and T_o is the reference temperature. As a final check, we operated the tunnel with the gradient in the opposite direction (warm air below) and found that the results were consistent with the case in which the warmer air was above. Thus, temperature was indeed a passive scalar. We will return to the mean scalar field in §3.

The velocity fluctuations were measured with with a TSI 1210 single-wire probe or a TSI 1241 X-probe. Velocity calibration followed the method of Browne, Antonia & Chua (1989) using an effective angle between the wire and the streamwise direction. The separation between the two wires of the X-wire was 0.5 mm. When simultaneous velocity and temperature measurements were made, the temperature wire was spaced 0.5 mm from the X-wire and compensation to the velocity for temperature fluctuations (by a modified King's law with temperature dependent coefficients) followed the method of Lienhard (1988). Tungsten wires of 3.05 μm diameter with a length to diameter ratio of approximately 200 were operated at an overheat of 1.8 using Dantec 55M01 constant-temperature anemometers. Tunnel and electronic noise were subtracted from the spectra on a mean-square basis. Spatial resolution corrections for wire length were made using the method of Wyngaard (1968).

The temperature fluctuations were measured with a TSI 1210 single-wire probe. Platinum resistance wires of 0.63 μm diameter were used. Their length to diameter ratio, L/d_w, where L is the etched length of the wire and d_w is the wire diameter, varied between 500 and 650. The minimum prong spacing was roughly $3L$. They were operated at low overheat (probe current approximately 250 μA) to minimize

contamination by velocity. Electronic and ambient thermal noise were subtracted from the spectra on a mean-square basis. Spatial resolution corrections for wire length were made using the method of Wyngaard (1971). Transverse temperature derivative measurements were made using a pair of sensors in the same manner as described in Tong & Warhaft (1994).

The highest frequency of each flow ($f_\eta \equiv U_o/(2\pi\eta)$) is listed in table 1. For the cases performed in the horizontal wind tunnel, f_η was generally within the -3 dB point constraints of LaRue, Deaton & Gibson (1975) for new 0.63 μm diameter cold wires. At our largest Reynolds numbers in the vertical wind tunnel, where all the (physical) scales are smaller than in the horizontal wind tunnel (since the mesh spacing is smaller in the vertical tunnel), f_η exceeded these constraints for the highest mean speeds (i.e. $U_o > 10$ m s^{-1}). Yet there exists ample evidence suggesting that the interpretation of our results is not affected for these measurements. We observed close consistency in our results between the horizontal and vertical wind tunnels (in which the sampling frequencies are significantly different) for all statistics. These include, for example, skewnesses, kurtoses, etc. of the scalar derivative and the expectations of temperature differences conditioned on the dissipation. We also show that in the dissipation range of frequencies, the temperature spectrum exhibits a 'spectral bump' which increases in magnitude with Reynolds number. If our cold wires were plagued with serious temporal resolution problems, the spectral bump would be attenuated away as the Reynolds number was increased. (We also note that the frequency response of our electronics was more than adequate – the -3 dB point of the frequency response of our fast-response DC temperature bridges (based on the design of Haughdal & Lienhard, 1988) was now 25 kHz after having been modified for an improved frequency response by using new OP37 (Analog Device) operational amplifiers.)

For cold wire lengths of $L/d_w < 1500$, Browne & Antonia (1987) show that heat conduction between a cold wire and its stubs and/or prongs is a significant source of error in the moments of temperature and its time derivative. Unfortunately, minimization of this error by use of a longer wire results in an increase in error from the reduced spatial resolution of the wire. Larger L/d_w could be achieved by use of a wire of smaller diameter – wires of 0.25 μm have been used – but would be at the expense of extreme wire fragility. A typical value of η_θ for our flow was 0.3 mm. Using 0.63 μm diameter wire of length $L = 1500d_w$ then results in a value of η_θ/L of 0.32. Wyngaard (1971) estimates that at this value of η_θ/L, the scalar dissipation would be underestimated by roughly 30%. We measured temperature spectra and moments (simultaneously) with two wires – one with an L/d_w ratio of 560, the other of 960. The spectra for each wire overlayed almost exactly except for a divergence at high wavenumbers which resulted in a reduction of the dissipation for the longer wire. Our results for the moments of temperature are qualitatively similar to those given by Browne & Antonia (1987): the second and fourth moments of the fluctuating temperature were higher for our longer wire by 4% and 8% respectively. But this was not the case for the temperature derivative statistics – increasing our wire length did not improve the derivative statistics. We observed smaller values for the moments of temperature derivative for the longer wire (as would be expected from having observed the spectra). The second and fourth moments of the fluctuating temperature derivative were lower for the longer wire by 10% and 24% respectively. This indicates that spatial resolution is the dominant source of error for the derivative statistics in our flow. Considering our interest in both temperature and temperature derivatives, we are satisfied with our choice of wire length. In addition, the appropriate non-dimensionalizations are made to cancel error from either source wherever possible.

Speed (m s^{-1})	3.3	3.3	6.0	3.3	11.4	7.0	6.9
Mode	Synchronous	Synchronous	Synchronous	Random	Random	Random	Random
Tunnel	Vertical	Horizontal	Horizontal	Horizontal	Vertical	Horizontal	Horizontal
x/M	68	62	62	62	68	62	31
β (°C m^{-1})	4.8	2.5	3.7	2.7	3.6	3.6	5.1
ν (m^2 s^{-1})	16×10^{-6}	15.5×10^{-6}	15×10^{-6}	16×10^{-6}	16×10^{-6}	16×10^{-6}	15×10^{-6}
$\langle u^2\rangle$ (m^2 s^{-2})	0.0156	0.0290	0.100	0.0911	1.04	0.583	1.44
$\langle u^2\rangle^{1/2}/U$ (%)	3.8	5.2	5.3	9.1	8.9	10.9	17.4
ϵ ($= 15\nu\int_0^\infty k_1{}^2F_{11}(k_1)\mathrm{d}k_1$) ($m^2$ s^{-3})	0.0314	0.0418	0.164	0.0833	6.13	0.940	3.88
ℓ ($= 0.9\langle u^2\rangle^{3/2}/\epsilon$) (m)	0.056	0.11	0.17	0.30	0.16	0.43	0.40
R_λ ($= \langle u^2\rangle\{15/(\nu\epsilon)\}^{1/2}$)	85	140	247	306	407	582	731
R_ℓ ($= \langle u^2\rangle^{1/2}\ell/\nu$)	440	1200	3600	5600	9900	20300	32100
η ($= (\nu^3/\epsilon)^{1/4}$) (mm)	0.60	0.55	0.38	0.47	0.16	0.26	0.17
ϵ_θ (see equation (8)) (°C^2 s^{-1})	0.124	0.277	0.581	0.799	0.466	1.74	4.96
$\langle\theta^2\rangle$ (°C^2)	0.062	0.176	0.336	0.800	0.080	1.07	2.05
ℓ_θ ($= \langle\theta^2\rangle^{1/2}/\beta$) (m)	0.052	0.17	0.16	0.33	0.079	0.29	0.28
n_1	1.36	1.48	1.53	1.54	1.54	1.58	1.60
n_θ	1.49	1.54	1.55	1.61	1.58	1.65	1.65
f_η ($= U/(2\pi\eta)$) (kHz)	0.88	0.95	2.5	1.1	11.3	4.3	6.5

TABLE 1. Flow parameters. These seven representative cases were selected from many more used to determine the flow evolution as a function of R_λ. n_1 and n_θ are the values of the scaling exponent for the u and θ spectra respectively (see text §4 for the way they were determined). The thermal diffusivity, κ, was 22.5×10^{-6} m^2 s^{-1}.

All signals were high- and low-pass filtered and digitized with a 12 bit A/D converter. From 4×10^5 to 8×10^5 samples were taken for each data record, rapidly (order of a Kolmogorov time period) for spectral measurements, but slowly (order of an integral time period) for the p.d.f. measurements to provide statistical independence.

3. Flow characteristics

Our initial objective was to study the mixing of temperature fluctuations in the presence of a constant cross-stream mean temperature gradient, $\beta(\equiv \partial T/\partial y)$, where y is in the direction of the gradient and the flow is in the x-direction. Corrsin (1952) showed that in isotropic turbulence, the mean temperature profile (β) should not decay with x. This follows from the enthalpy equation

$$U_0 \frac{\partial T}{\partial x} = \frac{\partial}{\partial y}(\kappa\beta - \langle \theta v \rangle), \tag{6}$$

where U_0 and T are the mean velocity (which is constant) and the mean temperature. The right-hand side of the above equation must be zero if the temperature profile is linear, the thermal diffusivity is constant and the turbulent heat flux is homogeneous in the transverse direction. A typical temperature profile in the tunnel at two downstream positions is shown in figure 1. While the linearity of the temperature gradient is good (its departure from linearity is much less than a standard deviation of the thermal fluctuations) we see that the gradient decays in the downstream direction. The weakening of the temperature gradient with x in the present work (figure 1) is due to the large integral length scale of the thermal (and velocity) field, ℓ_θ and ℓ respectively, generated by the active grid (see table 1). Because ℓ_θ is comparable to the tunnel size, the flow in some ways behaves like a thermal mixing layer which occurs at the interface of warm and cold constant-temperature flows (e.g. Ma & Warhaft 1986). Thus as the flow evolves, there is an upper (and lower) limit of temperature difference (corresponding to the highest and lowest temperatures in the tunnel, i.e. the air at the top and bottom of the tunnel) that a fluid particle arriving from upstream can have. For a mean streamline in the x-direction closer to the lower wall, the maximum temperature deficit of a fluid particle arriving from the cool part of the flow is of smaller magnitude than the maximum temperature excess of particles arriving from the warm part since the streamline is closer to the temperature minimum. Thus the temperature will increase along the mean streamline. Similarly for a mean streamline closer to the upper wall: the mean temperature will decrease with x. (The middle streamline will remain at constant temperature.) On the other hand, the ideal linear profile, approximately realized by Sirivat & Warhaft (1983) using a traditional passive grid, has an integral scale much smaller than the tunnel size. Therefore, from the point of view of an eddy, the tunnel would appear infinitely wide, and it would not feel the presence of the highest and lowest temperatures of the tunnel. Thus, the probability of a particle arriving with an excess or deficit in temperature is equal, so $\beta(x)$ is constant.

Because ℓ_θ is comparable to the tunnel width, the tails of the p.d.f. of temperature are weaker since very high temperature excursions do not occur. The p.d.f. is shown in figure 2 for the grid in random mode at $R_\lambda = 582$. The temperature p.d.f. is sub-Gaussian, with a kurtosis, $K_\theta \equiv \langle \theta^4 \rangle / \langle \theta^2 \rangle^2$ of 2.3. Such sub-Gaussian p.d.f.s (for a Gaussian p.d.f., $K_\theta = 3$) are also observed in thermal mixing layer experiments where a temperature gradient exists between regions of hot and cold air (e.g. Jayesh, Yoon & Warhaft 1991). The temperature p.d.f. in the present experiment should be contrasted

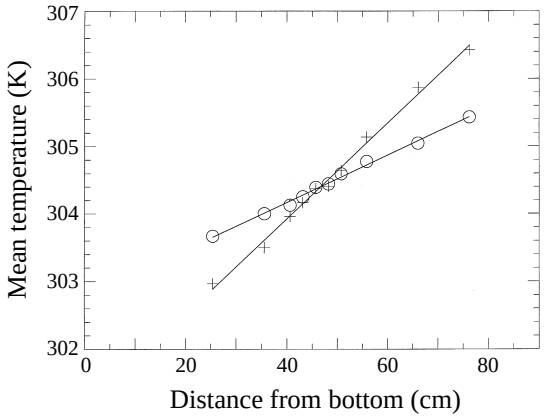

FIGURE 1. Typical mean temperature profiles in the wind tunnel at $x/M = 27$ ($\beta = 7.1$ K m^{-1}, plus signs) and $x/M = 53$ ($\beta = 3.6$ K m^{-1}, circles). $R_\lambda = 582$ (horizontal tunnel, random mode).

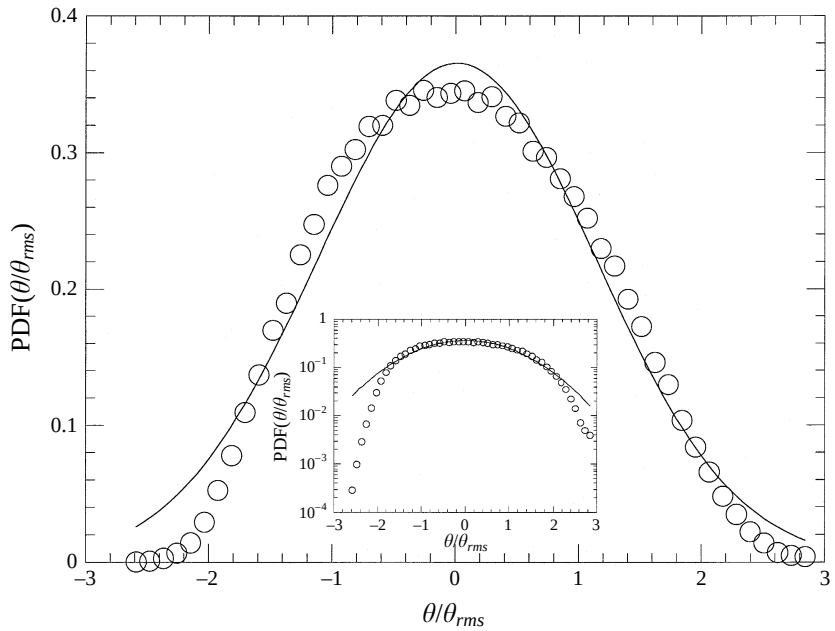

FIGURE 2. A typical probability density function (p.d.f.) of the temperature fluctuations (θ) normalized by their r.m.s. value (θ_{rms}). $S_\theta = 0.12$, $K_\theta = 2.31$. $R_\lambda = 582$ (horizontal tunnel, random mode). The solid curve is the best-fit Gaussian. The inset shows the same p.d.f. in log-linear co-ordinates.

to that studied (also for a mean temperature gradient) by Jayesh & Warhaft (1992). There the tunnel width was many integral scales wide and so rare events in which hot, or cold, fluid was transported to a mean streamline from far away in the transverse direction were possible. Here, super-Gaussian p.d.f.s were observed. (See Shraiman & Siggia 1994 for the physics of this anomalous diffusion process.)

The weakening of the temperature gradient with downstream distance was observed for the grid operated in both the random and synchronous modes, but was more pronounced for the former mode since here the value of ℓ_θ was larger (table 1). It

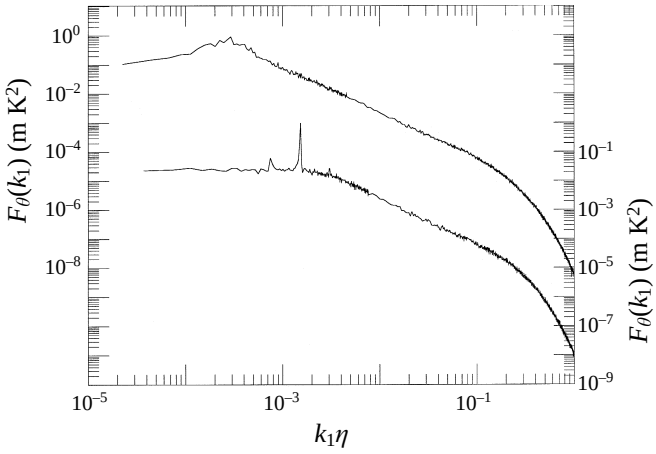

FIGURE 3. Typical temperature (θ) spectra, $F_\theta(k_1)$. Upper curve (left ordinate): $R_\lambda = 582$ (horizontal tunnel, random mode). Lower curve (right ordinate): $R_\lambda = 217$ (horizontal tunnel, synchronous mode). k_1 is the longitudinal wavenumber $= 2\pi f/U_\circ$. η is the Kolmogorov length scale $= (\nu^3/\epsilon)^{1/4}$.

occurred both in the vertical and horizontal tunnels since the ratio of ℓ_θ to the tunnel width was approximately the same.

As mentioned in §2, the new grid no longer produced a spike in the velocity spectrum since each bar's rotation rate was slightly offset from a nominal value. Still, this improvement did not eliminate the spike from the temperature spectra. Figure 3 shows temperature spectra for the new grid operating in both the random and synchronous modes. For all the measurements reported here, the nominal rotation rate of the grid bars for the active grid was either 1 or 2 revolutions per second. This frequency was always below the frequency corresponding to the integral scale of the turbulence. The contamination of the temperature spectrum due to the grid bar rotation frequency in the random mode occurs over a range of frequencies since each bar's rotation rate was slightly offset from a nominal value to remove the spike from the velocity spectrum. In the synchronous mode, each bar rotated at the same frequency which resulted in a distinct spike. In the case of figure 3, there is a spike at $k_1\eta = 0.0015$, which corresponds to twice the rotation frequency (4 Hz $= 2 \times 2$ r.p.s. in this case), as well as a smaller spike at $k_1\eta = 0.00075$ (2 Hz) and a weak harmonic of the large spike. (Operating the grid in a synchronous fashion by rotating each bar at a slightly different speed without it changing directions was impractical since it resulted in a periodic fluctuation of the integral scale with time as the bars would fall in and out of phase with each other.) Energy spectra (not shown) can be plotted by multiplying the power spectra of temperature by k_1. Their peak provides an estimate of the integral scale. The spikes were found to occur at scales larger than the integral scale. For this reason, and the fact that the statistics were independent of the mode of operation of the grid, we argue that the spikes do not contaminate the inertial and dissipation range statistics.

We note that to accurately determine the spectra (of velocity or temperature) over the whole range of scales, we were required to measure the spectra in two steps. The high-frequency portion of the spectrum was first measured by low-pass filtering at a frequency slightly larger than the Kolmogorov microscale, and then sampling at twice this frequency. This would resolve well the smallest scales of the spectra, but due to the broad range of scales in our high-Reynolds-number flow, our largest scales

were not well resolved. The low-frequency portion of the spectra was measured by setting the low-pass filter frequency to an intermediate value (generally in the inertial range) and sampling at twice this frequency. The longer data sets (due to the slower sampling frequency) now resolved the largest scales well. The two spectra were then blended to produce the final spectrum. This would result in a decrease in scatter in the middle of the final spectrum (see figure 3, for example) where the transition in the two sampling frequencies occurred since the point density in our spectra changes with the sampling frequency.

In summary, the attainment of the high Péclet number has had some cost on the bulk structure of the scalar field as we had ideally envisaged it: its mean gradient decays with x and the scalar p.d.f. is sub-Gaussian. Nevertheless, the small-scale and inertial-range scalar characteristics are unaffected by this. We will show that our active grid results at low Pe are similar to those of a conventional grid (with a small integral scale to tunnel width ratio) and those at high Pe are similar to those measurements in geophysical and high-Pe laboratory shear flow experiments. Thus the large-scale features of the mean scalar field do not appear to affect the intermediate- and small-scale scalar characteristics, which we will show are universal. Finally, we note that the tunnel walls do not affect the velocity field: it is very close to Gaussian (M&W figure 5) and is very nearly isotropic at the integral scale.

4. Results

We will report results which span the Reynolds number range $30 < R_\lambda < 731$. Three types of measurements are presented. The first type is temperature structure function measurements in which the separation of two temperature wires is systematically varied (along the mean temperature gradient) from small to integral scale spacings. This type of measurement spanned the range $99 < R_\lambda < 461$. The second type is transverse temperature derivative measurements in which two temperature wires are very closely spaced (i.e. $\Delta/\eta \approx 1$, see Tong & Warhaft 1994.) This type spanned the range $88 < R_\lambda < 731$. (These measurements are supplemented by the transverse temperature derivative results of Tong & Warhaft 1994 which spanned the range $30 < R_\lambda < 130$.) The last type of measurement presented corresponds to turbulent heat flux measurements in which velocity and temperature fluctuations were simultaneously made (measured with an X-wire and a temperature wire respectively). These spanned the range $85 < R_\lambda < 582$. We will begin by presenting further results on the velocity field (§4.1) obtained with our new active grid. We then report our findings for the scalar in terms of its spectra (§4.2), its structure functions (§4.3), its fine-scale structure (§4.4) and conditional statistics (§4.5).

4.1. *New results on the velocity field*

The construction of our new, larger active grid for our horizontal tunnel has permitted us to achieve even higher turbulent Reynolds numbers than we had achieved in M&W. Figure 4 shows a longitudinal velocity spectrum for $R_\lambda \equiv \langle u^2\rangle^{1/2}\lambda/\nu = 671$. Here, as in M&W, λ is defined as $\lambda \equiv [\langle u^2\rangle/\langle(\partial u/\partial x)^2\rangle]^{1/2}$. The insert (figure 4) shows the same spectrum multiplied by ${k_1}^{n_1}$, where n_1 is determined by trial and error such that the resulting 'optimally compensated' spectrum has a horizontal plateau. This plateau signifies the extent of the scaling region and n_1 gives its slope. In this case, it is 1.61, still below Kolmogorov's prediction of 5/3, but in good agreement with the empirical fit of equation (15) from M&W which showed that $n_1 = 5/3 - 5.25R_\lambda^{-2/3}$.

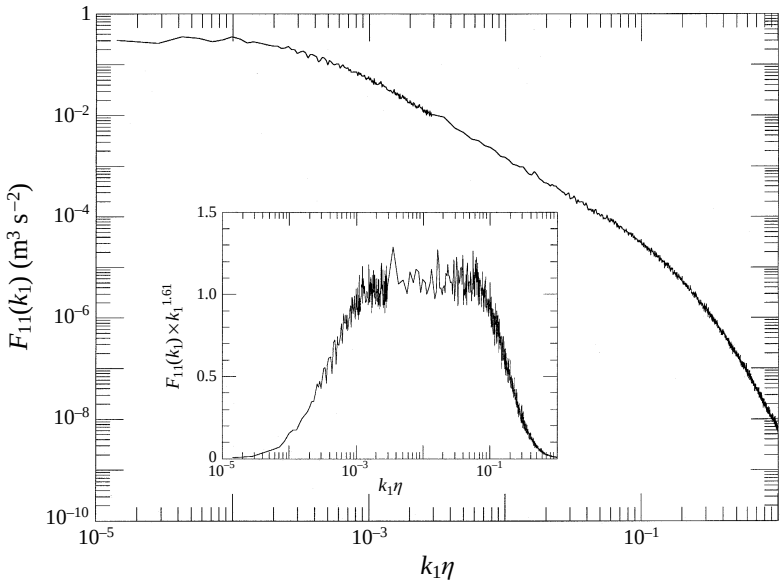

FIGURE 4. A longitudinal velocity (u) spectrum, $F_{11}(k_1)$. $R_\lambda = 671$ (horizontal tunnel, random mode). The insert shows the same spectrum multiplied by $k_1^{1.61}$.

The modified Kolmogorov variable, C_{1*}, defined by $F_{11}(k_1) = C_{1*}\epsilon^{2/3}k_1^{-5/3}(k_1\eta)^{5/3-n_1}$, is found to be 0.64, also in good agreement with the extrapolation of the data of M&W. The new higher-Reynolds-number data also agree extremely well with the conditional statistics of velocity differences for the highest-Reynolds-number data ($R_\lambda = 473$) of M&W (see their figures 26–28). For this flow, the intermittency exponent (defined in §4.5 below) was found to be 0.13. In general, the new data smoothly follow all the trends with Reynolds number observed in M&W.

4.2. *The scalar spectra*

In figure 3, we showed typical spectra for the tunnel operating in both random and synchronous modes. Both have significant inertial subranges, nearly two decades wide for the highest R_λ. Spikes due to the effects of the grid rotation are evident at the low-wavenumber regions of the spectra. These have been discussed in §3.

In order to plot the temperature spectrum in the form of equation (2), ϵ and ϵ_θ (equations (4) and (5)) must first be determined. As in M&W, ϵ was estimated as $\epsilon = 15\nu\int_0^\infty k_1^2 F_{11}(k_1)\mathrm{d}k_1$. This assumes isotropy in the velocity field – a sound assumption at least for second-order quantities such as ϵ (M&W; Saddoughi & Veeravalli 1994). As mentioned in the introduction, the small-scale temperature gradient field was determined to be anisotropic. Figure 5 shows the ratio $\langle(\partial\theta/\partial y)^2\rangle^{1/2}/\langle(\partial\theta/\partial x)^2\rangle^{1/2}$ as a function of R_λ. Its value is 1.2 ± 0.1 and appears to be independent of R_λ. For these measurements, the wire spacings were varied over the range $\Delta/\eta = 1$ to $\Delta/\eta = 4$, with no apparent effect on these results. Our present results are consistent with Tong & Warhaft (1994) and with other isolated measurements (at single values of R_λ) by Budwig, Tavoularis & Corrsin (1985) and Thoroddsen & Van Atta (1996). (The latter was for a stratified flow, but the measurements close to the grid are passive.) We will discuss the anisotropic nature of the thermal field in more detail below. Our purpose here is to arrive at an estimate of ϵ_θ.

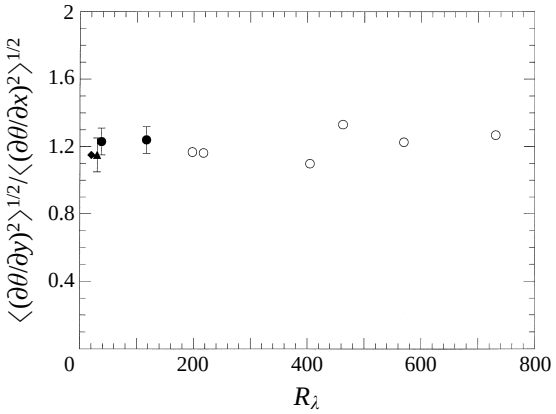

FIGURE 5. The ratio of the transverse to longitudinal temperature derivative standard deviations as a function of R_λ. Solid circles are the data of Tong & Warhaft (1994) who used a conventional grid. The solid diamond corresponds to the work of Thoroddsen & Van Atta (1996). The solid triangle corresponds to the work of Budwig *et al.* (1985). Open circles are for the present work using the active grid.

Figure 5 shows that

$$\left\langle \left(\frac{\partial\theta}{\partial y}\right)^2 \right\rangle = 1.4 \left\langle \left(\frac{\partial\theta}{\partial x}\right)^2 \right\rangle \tag{7}$$

with an error of approximately ± 0.2. Since the anisotropy is constant with R_λ (figure 5), we have determined ϵ_θ, using the above equation and our observation that $\langle(\partial\theta/\partial x)^2\rangle = \langle(\partial\theta/\partial z)^2\rangle$ (i.e. that the anisotropy is confined to the direction of the temperature gradient), to be

$$\epsilon_\theta = 6.8\kappa \left\langle \left(\frac{\partial\theta}{\partial x}\right)^2 \right\rangle. \tag{8}$$

For an isotropic temperature field,

$$\epsilon_\theta = 6\kappa \left\langle \left(\frac{\partial\theta}{\partial x}\right)^2 \right\rangle. \tag{9}$$

We now turn to the temperature spectra themselves. In figure 3, we have shown that the temperature spectrum has a significant scaling range: it appears to be nearly two decades for the largest Péclet number. In figure 6, we have plotted a typical temperature spectrum ($R_\lambda = 582, Pe_\lambda = 414$) compensated (in the manner implied by KOC scaling theory) by multiplying it by $k_1^{5/3}$. (In this figure, the low-wavenumber contamination from the grid bar rotation rates (§3) has been removed from the spectrum.) The occurrence of the horizontal plateau indicates the extent of the inertial range. Our normalization is such that the magnitude of the plateau is the Obukhov–Corrsin constant, C_θ (equation (2)). The spectrum indicates approximately one decade of inertial range followed by a significant bump before the dissipation range. The value of C_θ in figure 6 is approximately 0.54. If we had used the isotropic estimate of ϵ_θ (equation (9)), then C_θ would be 0.61. Other similar plots for different data sets at the highest Reynolds numbers showed C_θ to vary from 0.45 to 0.55.

Sreenivasan (1996) compiled existing data on the value of C_θ and concluded that it was between 0.3 and 0.5, though the scatter in the data ranged from 0.31 to

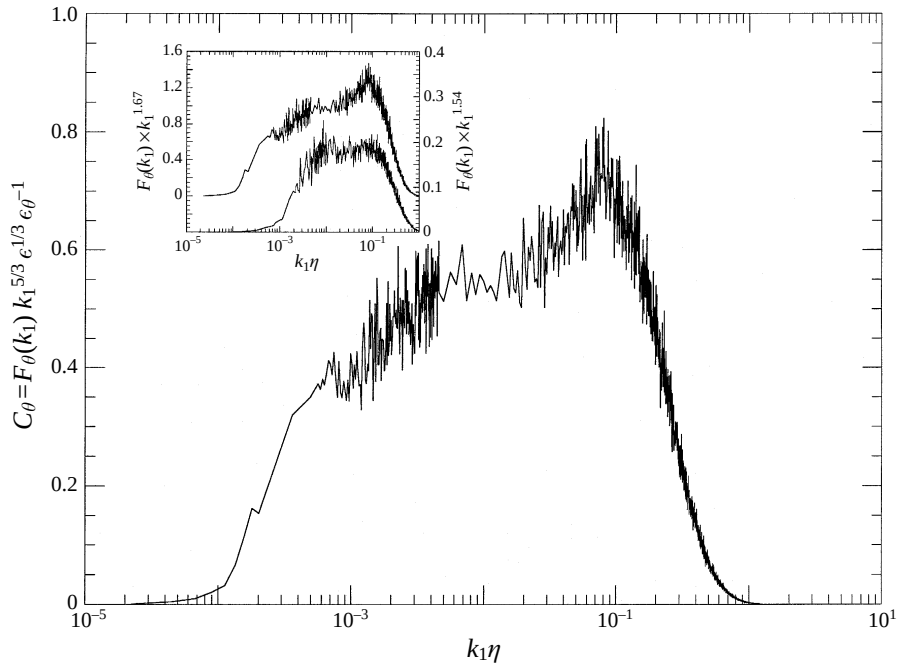

FIGURE 6. Compensated temperature (θ) spectrum, $F_\theta(k_1)k_1^{5/3}\epsilon^{1/3}\epsilon_\theta^{-1}$. $R_\lambda = 582$ (horizontal tunnel, random mode). The insert shows compensated temperature spectra for $R_\lambda = 140$ (horizontal tunnel, synchronous mode – lower curve, right ordinate) and $R_\lambda = 582$ (horizontal tunnel, random mode – upper curve, left ordinate). The increasing prominence of the spectral bump with R_λ is evident.

1.2. Sreenivasan's data were divided into two categories: data determined from grid-generated turbulence (values ranging from 0.33 to 0.6) and geophysical data (values ranging from 0.31 to 0.57 after having rejected some almost certainly erroneous data). The latter high-Reynolds-number data were the only type of shear flow data included since the slope of the inertial-convective region of the scalar spectrum in moderate and low-Reynolds-number ($R_\lambda < 2000$) shear flows is significantly below $-5/3$ (Sreenivasan 1991). In these compilations, no systematic effort was made to determine the value of ϵ_θ; in most cases, the thermal field was assumed isotropic. Yet both shear and shear-free turbulent flows at moderate Reynolds numbers have been shown to possess significant temperature derivative anisotropy (e.g. Sreenivasan, Antonia & Danh 1977 and Tong & Warhaft 1994, respectively). As we have shown above, it persists up to $R_\lambda \approx 730$ in our shear-free flow with no apparent Reynolds number dependence. Nevertheless, our value of 0.45 to 0.55 agrees with the (broad) range of estimates by Sreenivasan.

Shown in the insert of figure 6 is the same spectrum compared with a temperature spectrum at the lower R_λ of 140. Here, optimal compensation (to produce a horizontal plateau) was $F_\theta(k_1) \times k_1^{1.54}$. (We will show in a moment that there is a slight R_λ dependence of the slope of the spectrum.) As previously noted, the temperature spectrum at the higher Reynolds number has a distinct bump. There may exist a slight bump at the lower Reynolds number as well, but it is certainly much less evident. Such bumps in the spectrum of the scalar have been previously observed (e.g. Champagne *et al.* 1977 and Williams & Paulson 1977) and subsequently modelled (e.g. Hill 1978; Mestayer, Chollet & Lesieur 1983 and Tatarskii *et al.* 1992). The

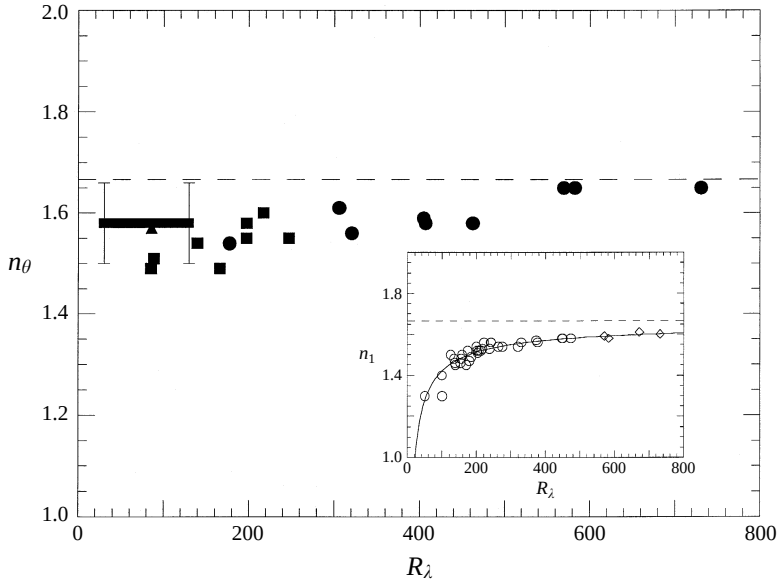

FIGURE 7. The slope, n_θ, of the temperature spectrum, $F_\theta(k_1)$, as a function of R_λ. Solid circles and squares are for the grid operated in the random and synchronous modes respectively. The thick line with the error bars represents the data of Jayesh *et al.* (1994) with a conventional grid, as is the solid triangle (present work). The insert shows the data of M&W for the slope of the longitudinal velocity spectrum, n_1, as a function of R_λ (open circles) with new data from the present work extending to higher R_λ (open diamonds). The thin solid line is the best fit curve of n_1 versus R_λ (see M&W, figure 10*a* and equation 15). Both dashed lines are 5/3.

spectral bump for the velocity field has been modelled by Lohse & Müller-Groeling (1996). The velocity spectrum does not appear to show a bump for any Reynolds number obtained in our flow (see insert in figure 4). Whether the appearance of a bump in the velocity spectra of other flows (e.g. Saddoughi & Veeravalli 1994 or Mestayer 1982) is attributable to the presence of mean shear, or whether it is simply due to over-compensation of the spectrum by use of a 5/3 scaling exponent rather than a smaller value is unclear (particularly since M&W suggest that a true 5/3 scaling exponent for the velocity field would not occur until $R_\lambda \sim 10^4$, a much higher Reynolds number than Saddoughi & Veeravalli 1994 or Mestayer 1982 achieve).

The temperature spectrum (figure 6) is for $R_\lambda = 582$. As in M&W, we studied the evolution of the spectra over a wide range of Reynolds numbers. In particular, we were interested to determine how n_θ, the slope of the scaling range in the temperature spectrum, varied with R_λ. As in M&W, the value of n_θ was determined by optimally compensating the spectrum by trial and error to produce a horizontal scaling region. In figure 7, we plot our measured n_θ over the range $85 < R_\lambda < 731$. Data for both the synchronous and random modes have been included as have data measured in our vertical wind tunnel with a standard two inch mesh grid. Shown in the insert to figure 7 are the data from M&W for the scaling exponent of the longitudinal velocity, n_1, to which are added new higher-Reynolds-number data from the present work. Also plotted is the best fit curve for the scaling exponent, n_1 (as determined in M&W). The new data follow extremely well the curve fit of M&W which was calculated from data with a maximum R_λ of 473. The departure in n_θ from the theoretical value of 5/3 decreases slightly with increasing Reynolds number, but is significantly closer

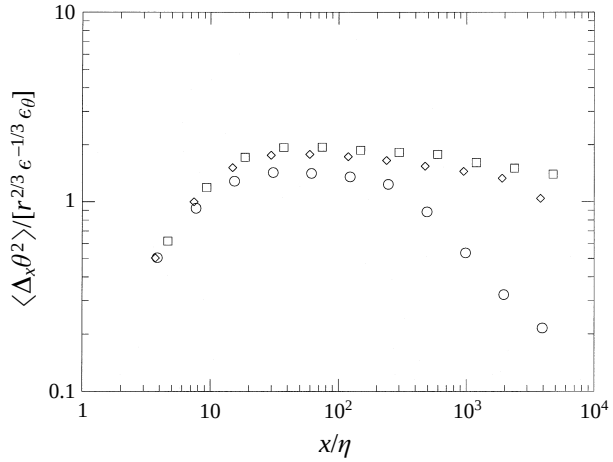

FIGURE 8. Compensated longitudinal second-order temperature structure functions, $\langle(\Delta\theta(x))^2\rangle/(\epsilon_\theta\epsilon^{-1/3}r^{2/3})$. Circles are for $R_\lambda = 89$ (vertical tunnel, synchronous mode). Diamonds are for $R_\lambda = 320$ (horizontal tunnel, random mode). Squares are for $R_\lambda = 569$ (horizontal tunnel, random mode).

to the value of 5/3 for all Reynolds numbers than is the scaling exponent of the longitudinal velocity power spectrum, n_1, at the corresponding Reynolds number.

Figure 7 shows that even at our lowest R_λ (less than 100), n_θ has a value of 1.5. This is consistent with the work of Jayesh *et al.* (1994) who found a scaling exponent of 1.58 ± 0.08 over the range $60 < R_\ell < 1200$ (which roughly corresponds to $30 < R_\lambda < 130$) in conventional grid turbulence. We find a slight upwards trend with R_λ. It is important to emphasize that for low R_λ, the velocity spectrum barely exhibited a scaling range, and when it did emerge at $R_\lambda \sim 50$, its slope was around 1.3. A value of 1.5 was not reached until roughly an R_λ of 200. At this larger Reynolds number, M&W observed a qualitative change in the nature of the turbulence for the velocity (from what they called *weak turbulence* to *strong turbulence*). Strong turbulence was characterized by the p.d.f.s of $\Delta u(r)$ and $\Delta v(r)$ (where r is an inertial-subrange distance) having super-Gaussian tails and the (surrogate of the) volume-averaged dissipation conditioned on both $\Delta u(r)$ and $\Delta v(r)$ being a strong function of the velocity difference. Since the scalar spectral exponent is close to 5/3 essentially for all Reynolds numbers, one could expect that the scalar fluctuations might possess the characteristics of strong turbulence at lower Reynolds numbers than for the velocity field. This will be shown to be the case in §4.5.

The longitudinal second-order temperature structure function, $\langle(\Delta\theta(x))^2\rangle$, normalized as given by KOC scaling theory is shown in figure 8. From this, the Obukhov–Corrsin constant can also be estimated. The universal constant for the longitudinal temperature structure function is (Monin & Yaglom, 1975)

$$C'_\theta \equiv \frac{\langle(\Delta\theta(x))^2\rangle}{\epsilon_\theta\epsilon^{-1/3}r^{2/3}}. \tag{10}$$

This is related to C_θ (equation (2)) by (Monin & Yaglom 1975)

$$C_\theta = \frac{2}{3\Gamma(\frac{1}{3})} \approx 0.25C'_\theta. \tag{11}$$

C'_θ from figure 8 is approximately 2 at the highest Reynolds number, yielding a value

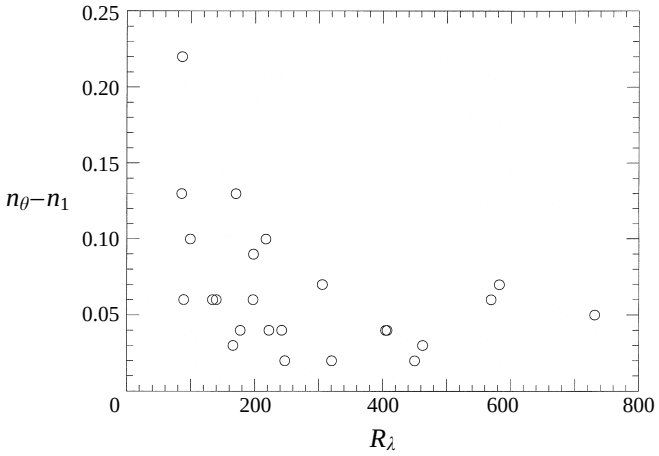

FIGURE 9. The difference between the temperature and longitudinal velocity scaling exponents, $n_\theta - n_1$, as a function of R_λ.

of $C_\theta \sim 0.5$ which agrees well with the results from figure 6. Again, we have used the relation (8) to determine ϵ_θ. An obvious trend is visible in this figure as the inertial range in the structure function develops with Reynolds number.

In figure 9, we plot $n_\theta - n_1$ as a function of Reynolds number. The scatter reflects the difficulty in determining n_θ and n_1 by the method of trial and error compensation. The difference between the slope of the temperature and streamwise velocity spectra is seen to be a strongly decreasing function of Reynolds number. Though it is still non-zero for our highest Reynolds numbers, the difference from zero is small. The notable feature of this plot is the significant value of $n_\theta - n_1$ for $R_\lambda < 200$. This suggests a fundamental difference between the turbulence of the velocity and the scalar fields at these lower Reynolds numbers.

Owing to the temperature gradient, there will exist a turbulent heat flux and hence a cospectrum, $F_{v\theta}(k_1)$, between the transverse velocity fluctuations, v, and the temperature fluctuations, θ. Figure 10 shows such cospectra for a low and a high Reynolds number ($R_\lambda = 140$ and $R_\lambda = 582$). These are plotted in optimally compensated form, i.e. multiplying by $k_1^{n_{v\theta}}$ where $n_{v\theta}$ is determined by trial and error such that it provides a horizontal scaling region. Also shown in figure 10 are optimally compensated temperature spectra at the same R_λ. The heat flux spectra are noisier than the temperature spectra since there is no mathematical limitation to prevent them from changing sign. To plot them in logarithmic coordinates, the occasional negative excursions have been removed. Dimensional analysis (Lumley 1967) predicts that the heat flux spectrum should be proportional to $k_1^{-7/3}$. The highest value of $n_{v\theta}$ in figure 10 is 2.0, significantly below 7/3 (= 2.33). A plot of the spectral exponent for the heat flux cospectrum as a function of R_λ is shown in figure 11. At the lowest R_λ, $n_{v\theta}$ is roughly 1.8 and it rises to a value of 2 by our highest Reynolds number.

We note that the bump in the temperature spectrum is not visible for the high-Reynolds-number case in figure 10 since the ordinate is plotted on a logarithmic scale. It is indeed there, as can be seen in figure 6. We do not observe a bump in the turbulent heat flux cospectrum for any of our Reynolds numbers, though when the ordinate is plotted on a linear scale the scatter is considerable.

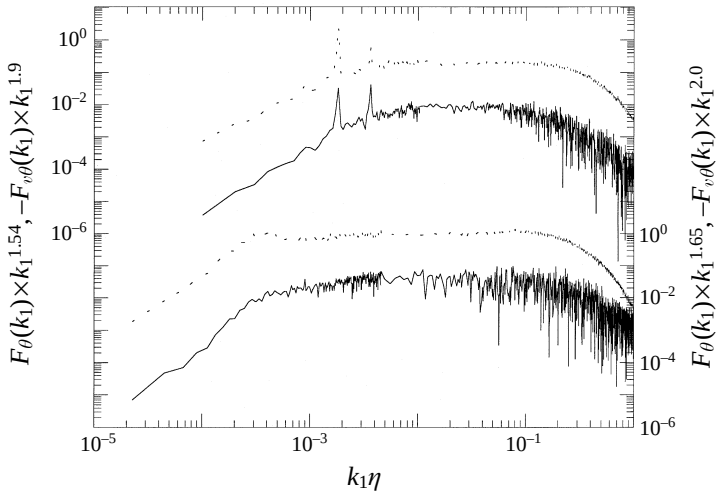

FIGURE 10. Optimally compensated temperature spectra and (negative of the) turbulent heat flux cospectra for $R_\lambda = 140$ (horizontal tunnel, synchronous mode – upper two curves (left ordinate): $n_\theta = 1.54$, $n_{v\theta} = 1.9$) and $R_\lambda = 582$ (horizontal tunnel, random mode – lower two curves (right ordinate): $n_\theta = 1.65$, $n_{v\theta} = 2.0$). Heat flux spectra (solid lines) are shifted down by one decade with respect to their corresponding temperature spectra.

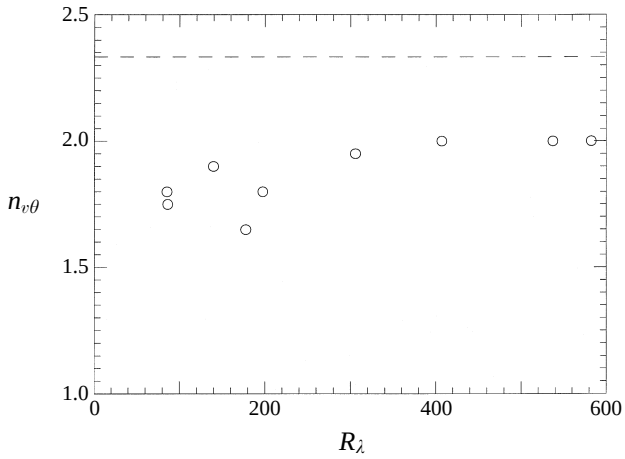

FIGURE 11. The slope, $n_{v\theta}$, of the turbulent heat flux cospectrum, $F_{v\theta}(k_1)$, as a function of R_λ. The dashed line is 7/3.

In M&W, we showed that the v spectral exponent developed slower (with R_λ) than the u spectrum (and both develop more slowly than the θ spectrum – figure 7 of the present work). It is reasonable to suppose that the slow $v\theta$ spectral exponent evolution is determined by the slow v spectrum development. Notice that our results suggest that (figure 11) if $n_{v\theta} \to 7/3$, it would be at extremely high R_λ, since its change with R_λ is very slow. It is also worth noting that a related quantity, $F_{uv}(k_1)$, the uv cospectrum, was measured by Saddoughi & Veeravalli (1994) in a boundary layer for $500 \leqslant R_\lambda \leqslant 1450$. They argue that the shear-stress spectrum, $F_{uv}(k_1)$, has a 7/3 slope even by $R_\lambda \sim 500$ although they do not plot it in compensated form.

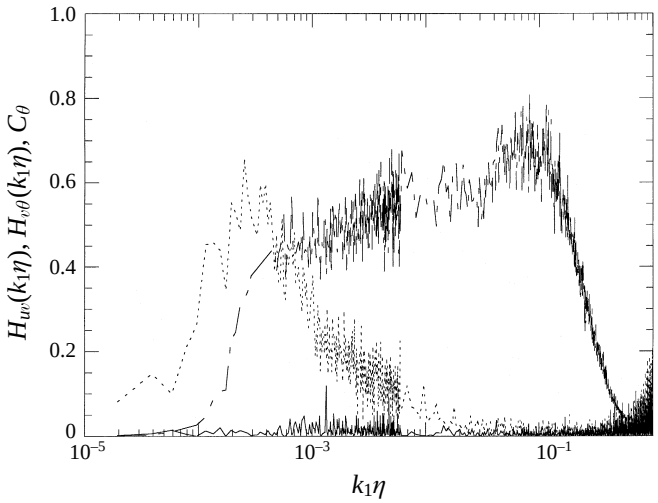

FIGURE 12. The coherence between v and θ, $H_{v\theta}$, for $R_\lambda = 537$ (horizontal tunnel, random mode; dashed line). Also shown is H_{uv} (solid line) which is essentially zero. The curve with the plateau is the compensated temperature spectrum. The plateau indicates the inertial–convective range.

An indication of the correlation between θ and v is given by the coherence (Bendat & Piersol 1986)

$$H_{v\theta} \equiv \frac{F_{v\theta}{}^2(k_1) + Q_{v\theta}{}^2(k_1)}{F_{22}(k_1)F_\theta(k_1)}, \tag{12}$$

where $F_{v\theta}(k_1)$ and $Q_{v\theta}(k_1)$ are the cospectrum the quadrature spectrum respectively. In figure 12, $H_{v\theta}(k_1)$ is plotted with a compensated temperature spectrum for the grid operated in random mode at an R_λ of 537. The coherence of v and θ falls to zero by $k_1\eta = 0.03$, showing that there is heat flux at inertial convective-subrange wavenumbers. This is analogous to Saddoughi & Veeravalli (1994) who found the Reynolds shear stress spectrum also extended into the inertial subrange. Also shown is the coherence of u and v, $H_{uv}(k_1)$, which is essentially zero since the flow is isotropic.

We note that the turbulent heat flux correlation coefficient, $\rho_{v\theta} \equiv \langle v\theta\rangle/(\langle v^2\rangle^{1/2}\langle\theta^2\rangle^{1/2})$, varied from a value of -0.21 to -0.54 at our standard downstream locations of $x/M = 62$ or 68. The correlation coefficient was smaller when the decay of the mean temperature gradient was more severe (i.e. $\rho_{v\theta}$ was generally smaller when the grid was operated in the random mode where the decay of the mean temperature gradient is largest – see §3). We also noted that the correlation coefficient increased as we moved upstream (where the decay of the temperature gradient was less severe.) In fact, the coherence shown in figure 12 for an R_λ of 537 was recorded at $x/M = 31$ where $\rho_{v\theta}$ was -0.48. Sirivat & Warhaft (1983) found $\rho_{v\theta}$ to be between -0.6 and -0.7 for the range $40 < x/M < 160$ using standard grid turbulence with a linear mean temperature profile. We can obtain this value using the active grid in the synchronous mode at positions closer to the grid.

4.3. *The structure functions*

We will now discuss the transverse structure functions of temperature for the second, third, fourth and fifth orders. We present results for three Reynolds numbers: $R_\lambda = 99$, 222 and 461. The first two are for the vertical tunnel operated in the synchronous mode, and the third is for the vertical tunnel operated in the random

mode. Figures 13(*a*)–13(*d*) show the second- to fifth-order transverse (y-direction, along the temperature gradient) structure functions. They are optimally compensated to produce a plateau in the inertial–convective subrange. Note that the existence of third- and fifth-order structure function is a violation of isotropy. This has previously been observed by Antonia & Van Atta (1978) and by Antonia *et al.* (1984) for shear flows, although there was not a systematic study of the R_λ dependence in their works. All second-order structure functions show a clear $r^{2/3}$ scaling region. The best-fit exponent to the scaling region for the third order was 0.9, 0.95, 0.85 (from lowest to highest Reynolds number); for the fourth order it was 1.0, 1.07 and 1.03 and for the fifth order it was 1.30, 1.30 and 1.15. Although there appears to be a slight trend for the odd-order structure functions to smaller scaling exponents for increasing R_λ, it is unclear whether this is significant or due to experimental scatter. The 2/3 power law dependence for the second-order structure function is expected by KOC arguments for inertial-subrange behaviour. The KOC scaling for any order structure functions is

$$\langle(\Delta u(r))^m(\Delta\theta(r))^n\rangle = C_{mn}\langle(r^{1/3}\epsilon^{1/3})^m(r^{1/3}\epsilon^{-1/6}\epsilon_\theta{}^{1/2})^n\rangle, \tag{13}$$

where C_{mn} are presumably universal constants dependent on the values of m and n. As the order rises, our measurements (figure 13) show that the exponents for the scaling regions increase at a lower rate than predicted by the above equation owing to the increasingly pronounced effect of the scalar internal intermittency. This has been previously observed by Antonia & Van Atta (1978) and by Antonia *et al.* (1984) for scalars in shear flows. For the even orders, our scaling exponents are consistent with the compilation of Antonia *et al.* (1984) (that includes the work of Antonia & Van Atta 1978) which shows a $r^{2/3}$ power law dependence for the second-order structure function and a r^1 dependence for the fourth order. For odd orders, our results are also consistent with Antonia & Van Atta (1978) who find a $\sim r^1$ dependence at the third order and a $\sim r^{1.3}$ dependence at the fifth order. (They do not compensate their structure functions nor do they give a best fit exponent in many cases.) It is remarkable that the third- and fifth-order structure functions are in sequence with the even-order structure functions. Note that for the lowest R_λ the scaling range is barely apparent, and it widens with increasing Reynolds number. This dilation with Reynolds number occurs in the same way for the odd-order structure functions as for the even-order ones.

Figures 14(*a*), 14(*b*) and 14(*c*) show the skewness, kurtosis and hyperskewness structure functions of the temperature difference. These are defined as

$$S_{\Delta_y\theta(r)} \equiv \frac{\langle\Delta_y\theta(r)^3\rangle}{\langle\Delta_y\theta(r)^2\rangle^{3/2}}, \tag{14}$$

$$K_{\Delta_y\theta(r)} \equiv \frac{\langle\Delta_y\theta(r)^4\rangle}{\langle\Delta_y\theta(r)^2\rangle^2} \tag{15}$$

and

$$HS_{\Delta_y\theta(r)} \equiv \frac{\langle\Delta_y\theta(r)^5\rangle}{\langle\Delta_y\theta(r)^2\rangle^{5/2}}. \tag{16}$$

As for the odd-order structure functions, if the scalar field were isotropic, the skewness and hyperskewness structure functions would be zero. This is not the case as can be seen in figures 14(*a*) and 14(*c*). The limit of these structure functions as the spacing tends to zero gives the derivative skewness and hyperskewness. They will be discussed in the following section. At the lowest Reynolds number ($R_\lambda = 99$, figure 14*a*), the

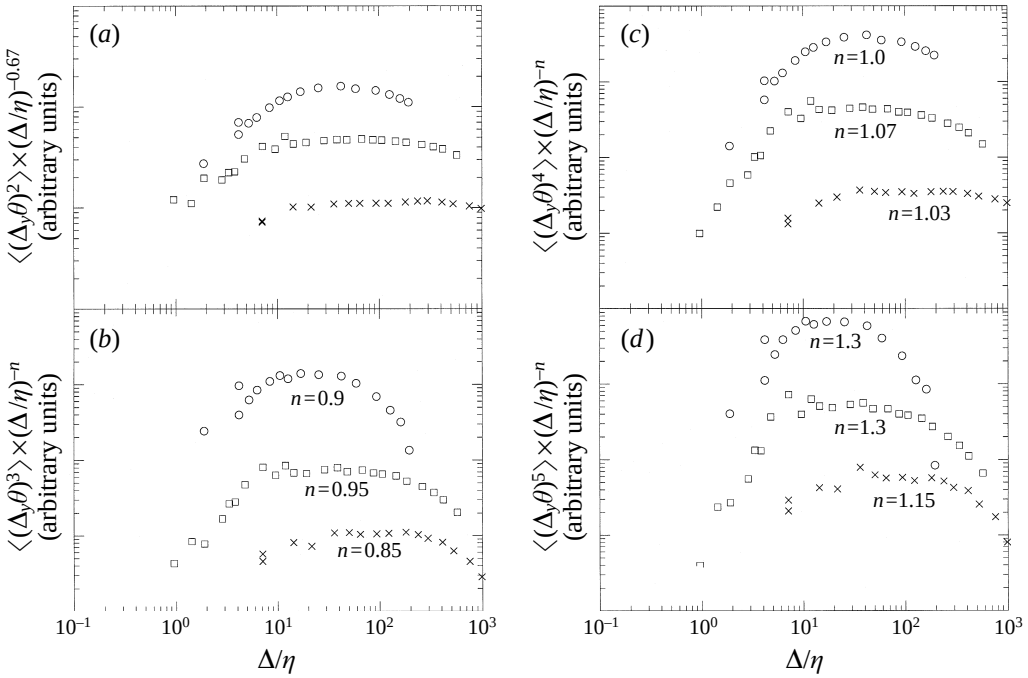

FIGURE 13. Optimally compensated transverse temperature structure functions $\langle(\Delta_y\theta)^m\rangle \times (\Delta/\eta)^n$ at the second ($m = 2$) order (*a*), third ($m = 3$) order (*b*), fourth ($m = 4$) order (*c*) and fifth ($m = 5$) order (*d*). The choice of n is made to produce a horizontal plateau in the inertial range and is shown on each figure. Circles are for $R_\lambda = 99$ (vertical tunnel, synchronous mode). Squares are for $R_\lambda = 222$ (vertical tunnel, synchronous mode). Crosses are for $R_\lambda = 461$ (vertical tunnel, random mode).

skewness of the temperature difference decreases with increasing spacing. At the higher Reynolds numbers, there exists a scaling region that is almost independent of the spacing (which agrees with the results of Mestayer 1982 for a heated boundary layer at $R_\lambda = 616$). This is what one would expect if the odd-ordered structure functions followed equations (13) and (14), namely, all normalized structure functions should be independent of the separation in the inertial range. Since isotropy predicts that the odd-ordered structure functions should not exist, we conclude that the plateau in this figure implies the coincidental scaling of the third-order structure function with the theory. This evolution implies, for the high Reynolds number, an independence of the skewness structure function of the separation.

In the inertial subrange, equations (13) and (15) also predict that the kurtosis should be independent of the separation, r. As can be seen from figure 14(*b*), the kurtosis structure function rises as the probe spacing is decreased from large separations where it has the Gaussian value of 3. This is due to the increasing effect of the internal intermittency of the scalar 'dissipation' as the scale is reduced. As a consequence, when the probe spacing is decreased, the p.d.f.s of the temperature difference lose their Gaussian shape and develop tails thus approaching derivative p.d.f.s (see e.g. M&W figure 24 for the equivalent effect on the velocity field). The best-fit exponent to the scaling region of the low- and high-Reynolds-number cases (figure 14*b*) was -0.45 and -0.37.

The data for the hyperskewness structure function shown in figure 14(*c*) collapse for the highest two Reynolds numbers as they did at the third order. Though, unlike

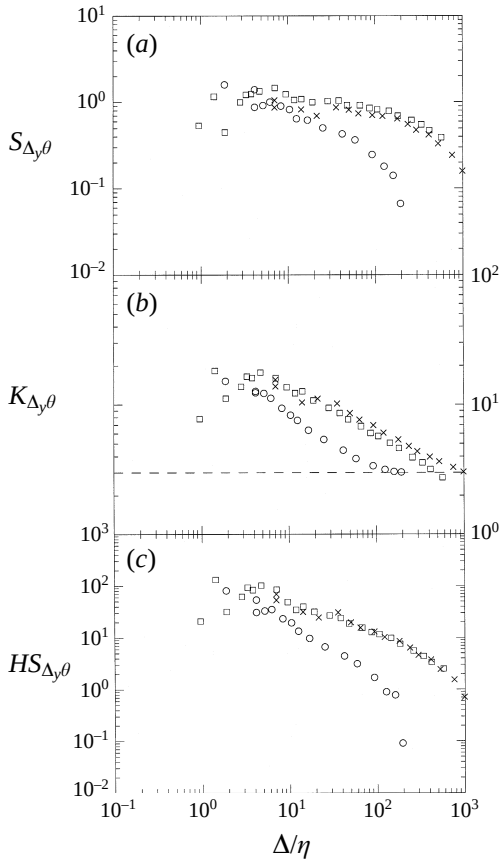

FIGURE 14. Normalized transverse temperature structure functions $\langle(\Delta_y\theta)^m\rangle/\langle(\Delta_y\theta)^2\rangle^{m/2}$ for the third ($m = 3$) order (a), fourth ($m = 4$) order (b) and fifth ($m = 5$) order (c). Same symbols as in figure 13.

the third order, the high Reynolds number data show a dependence on the separation. The best-fit exponent to the scaling region of the low and high Reynolds number cases was roughly -1 and -0.6. Antonia & Van Atta (1978) find the best-fit exponent in the inertial range of the hyperskewness structure function to be roughly -1. Since the existence of the odd-order structure functions violates basic KOC scaling theory, it is unclear whether this dependence should disappear at high Reynolds numbers.

The ratio of the transverse to longitudinal (even-order) structure functions is shown in figure 15 for $R_\lambda = 564$. In isotropic flow, this should be unity. We find this to be the case in the inertial subrange. But at the dissipation scales, we again find anisotropy. In the limit of zero separation, this plot shows the derivative anisotropy (at the second and fourth orders). These values are also shown on this figure. (For the second order, this is taken from figure 5.) It is particularly important to note that although the second-order structure function shows that the temperature difference is anisotropic at the small scale, in contrast to the odd-order functions, it is isotropic in the inertial subrange. We also note that the odd-order longitudinal structure functions (in the flow direction and thus normal to the temperature gradient) were zero, as they must be in a homogeneous and isotropic scalar field.

To investigate the dependence of temperature difference statistics in more than one dimension, we calculate what we call the nth-order diagonal structure functions of

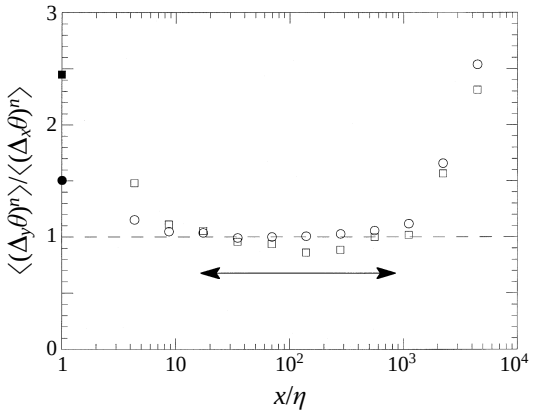

FIGURE 15. The ratio of the transverse to longitudinal (even-order) structure functions for $R_\lambda = 564$ (horizontal tunnel, random mode – open symbols). Circles are for the second order. Squares are for the fourth order. Solid symbols indicate the ratio of the transverse to longitudinal derivative variances. The horizontal arrow indicates the extent of the inertial–convective subrange determined from the second-order longitudinal structure function.

temperature:

$$\langle(\Delta_{x,y}\theta)^n\rangle \equiv \langle[\theta(x = Ut, y) - \theta(0,0)]^n\rangle. \tag{17}$$

Figures 16(*a*) and 16(*b*) respectively show the second- and fourth-order diagonal structure functions plotted for various separations. These data are collapsed by plotting them as a function of r/ℓ, where $r = (x^2 + y^2)^{1/2}$ and ℓ is the integral length scale defined as $\ell = 0.9\langle u^2\rangle^{3/2}/\epsilon$ (equation (12) of M&W). The lines fitted to the data show that the $r^{2/3}$ and the $r^{1.1}$ (inertial range) dependencies, displayed in figures 13(*a*) and 13(*c*) for the second and fourth orders, also hold in the plane defined by the transverse and longitudinal directions rather than only holding in one dimension. Indeed, in an isotropic field, these dependencies should hold in any direction, not just the longitudinal or transverse ones. We then see that, in this flow, structure function anisotropies are only apparent in the inertial subrange for odd orders.

The non-zero value of odd-order structure functions has been attributed to the 'ramp-cliff' large-scale coherent structures observed in the temperature signals in the direction of the temperature gradient (see, for example, Mestayer *et al.* 1976; Sreenivasan & Antonia 1977; Gibson, Friehe & McConnell 1977; Antonia & Van Atta 1978; Sreenivasan, Antonia & Britz 1979; Antonia *et al.* 1979; Mestayer 1982). In our flow, the temperature gradient is in the transverse (y) direction and therefore the ramps and cliffs must occur in this same direction. To observe these structures in our flow would then require a (spatial) trace of $\theta(y)$ which would require a large number of simultaneous measurements made by probes aligned in the y-direction. But the geometry of our flow does allow us to estimate their transverse width, which we will do in a moment.

In figure 17, we have plotted the diagonal third-order structure functions of temperature for various separations, y, against x/ℓ. Data are shown for values of y/ℓ ranging from 0.012 to 0.75 for $R_\lambda = 247$. It can be seen that the dependence on x is very weak, therefore larger amounts of data were required for convergence of these statistics: $3 \times 10^6 - 4 \times 10^6$ samples were recorded (i.e. 750–1000 blocks each composed of 4096 samples) for each transverse spacing. In addition, for reasons given in detail in Mydlarski & Warhaft (1997), these statistics should be even in the x

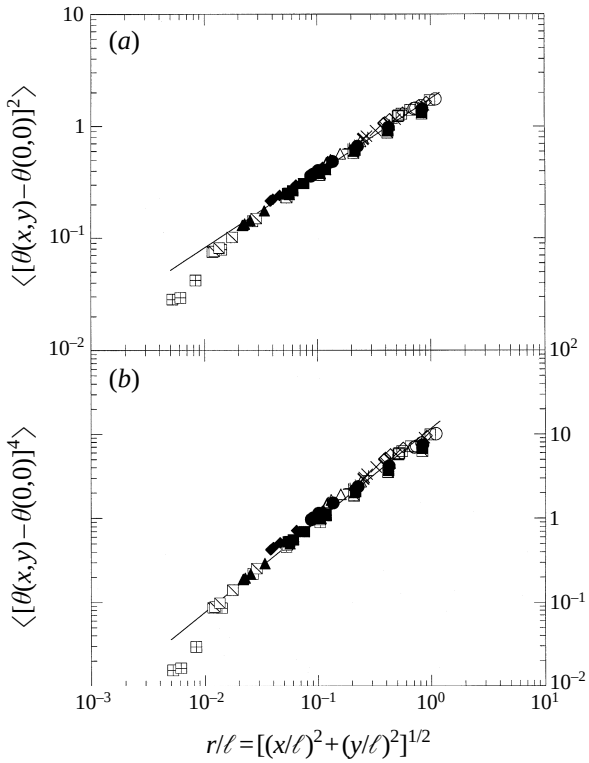

FIGURE 16. The diagonal even-order structure functions of temperature, $\langle(\Delta_{x,y}\theta)^n\rangle$, for $R_\lambda = 569$ (horizontal tunnel, random mode) as a function of r/ℓ, where $r = (x^2 + y^2)^{1/2}$ and ℓ is the integral length scale. In (*a*), $n = 2$ and the straight line is a $r^{2/3}$ power law. In (*b*), $n = 4$ and the straight line is a $r^{1.1}$ power law. Squares with plus signs are $y/\ell = 0.0052$; squares with backslashes are $y/\ell = 0.012$; solid triangles are $y/\ell = 0.022$; solid diamonds are $y/\ell = 0.038$; solid squares are $y/\ell = 0.055$; solid circles are $y/\ell = 0.088$; open triangles are $y/\ell = 0.12$; plus signs are $y/\ell = 0.19$; crosses are $y/\ell = 0.25$; open diamonds are $y/\ell = 0.38$; open squares are $y/\ell = 0.52$ and open circles are $y/\ell = 0.71$.

(longitudinal) direction. Any odd content (in the x-direction) can be attributed to non-inertial-range effects such as decay of the turbulence in the x-direction or very large-scale inhomogeneities in the flow. Therefore, in figure 17 (and 18) we have plotted the component of the statistic which is even in x, namely

$$\langle(\Delta_{x_{even},y}\theta)^3\rangle \equiv \tfrac{1}{2}(\langle(\Delta_{x,y}\theta)^3\rangle + \langle(\Delta_{-x,y}\theta)^3\rangle). \tag{18}$$

The data in figure 17 (and 18) is for a lower Reynolds number than that of figure 16, because we limited the wind tunnel operation to the synchronous mode (which has a smaller integral length scale) for these odd-ordered statistics since they are more sensitive to the large-scale inhomogeneities as alluded to in §3 and further discussed with respect to figure 22.

In the limit of zero separation in the x-direction, figure 17 simply shows the transverse third-order structure function of temperature. The value of $\langle(\Delta_{x_{even},y}\theta)^3\rangle$ can be seen to be constant up to $x/\ell \sim 1$, implying the width of a 'ramp-cliff' structure (where by 'width' we mean the size of the structure in the direction normal to the plane in which the ramp-cliff patterns occur) is on the order of an integral scale.

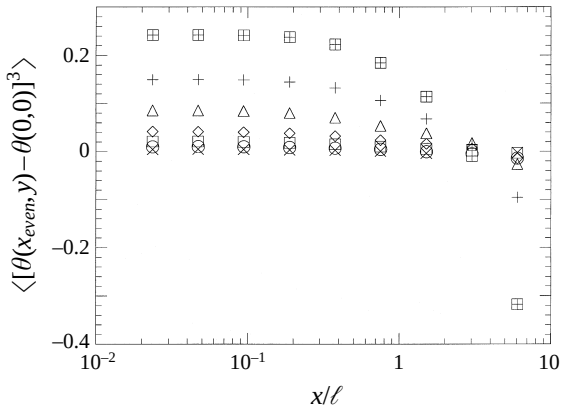

FIGURE 17. The component of the diagonal third-order structure functions of temperature which is even in x, $\langle(\Delta_{x_{even},y}\theta)^3\rangle$ for $R_\lambda = 247$ (horizontal tunnel, synchronous mode) plotted against x/ℓ ($x = Ut$). Crosses are $y/\ell = 0.012$; circles are $y/\ell = 0.024$; squares are $y/\ell = 0.047$; diamonds are $y/\ell = 0.094$, triangles are $y/\ell = 0.19$; plus signs are $y/\ell = 0.38$ and squares with plus signs are $y/\ell = 0.75$.

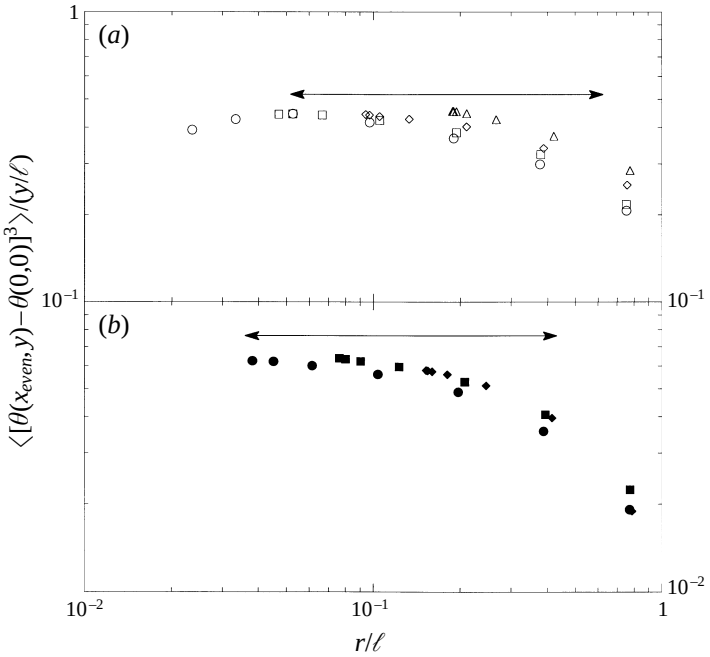

FIGURE 18. The component of the diagonal third-order structure function of temperature which is even in x, $\langle(\Delta_{x_{even},y}\theta)^3\rangle$ and scaled by y/ℓ, plotted as a function of r/ℓ, where $r = (x^2 + y^2)^{1/2}$, $x = Ut$ and ℓ is the integral length scale. In (*a*) $R_\lambda = 247$ (horizontal tunnel, synchronous mode): open circles are $y/\ell = 0.024$; open squares are $y/\ell = 0.047$; open diamonds are $y/\ell = 0.094$ and open triangles are $y/\ell = 0.19$. In (*b*) $R_\lambda = 336$ (vertical tunnel, synchronous mode): solid circles are $y/\ell = 0.038$; solid squares are $y/\ell = 0.076$ and solid diamonds are $y/\ell = 0.15$. The horizontal arrow indicates the extent of the inertial–convective subrange determined from the second-order longitudinal structure function.

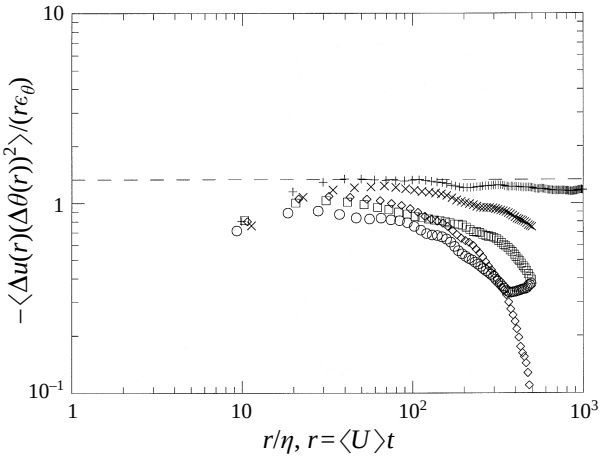

FIGURE 19. The compensated third-order combined velocity–temperature structure function, $-\langle(\Delta u(r))(\Delta\theta(r))^2\rangle/(r\epsilon_\theta)$. The symbols are circles: $R_\lambda = 85$ (vertical tunnel, synchronous mode), squares: $R_\lambda = 177$ (vertical tunnel, random mode), diamonds: $R_\lambda = 197$ (vertical tunnel, synchronous mode), crosses: $R_\lambda = 407$ (vertical tunnel, random mode) and plus signs: $R_\lambda = 582$ (horizontal tunnel, random mode). The dashed line is 4/3.

In figures 18(*a*) and 18(*b*), we have plotted, $\langle(\Delta_{x_{even},y}\theta)^3\rangle$, the diagonal third-order structure functions of temperature, scaled by y/ℓ since, in figure 13(*b*), we showed that the transverse third-order structure function scaled approximately as y. Here, we have shown two sets of data – one from each wind tunnel – to give an indication of the experimental scatter involved with this measurement. The resulting curves are flat for most of the inertial range, showing very little additional dependence on r and thus that the existence of the diagonal third-order structure function arises solely from structures in the direction of the gradient. (No dependence on x should be expected since the third-order longitudinal structure function is zero.) For the vertical tunnel data in figure 18(*b*), small inertial-range spacings have been omitted since accurate *in situ* probe separation measurements for these separations had larger relative error in that tunnel.

The third-order combined velocity–temperature structure function, $-\langle(\Delta u(r)) \times (\Delta\theta(r))^2\rangle$, is shown in figure 19. All differences are in the longitudinal direction. Unlike the second-order structure functions (or spectra), an exact, model-independent, expression for $\langle(\Delta u(r))(\Delta\theta(r))^2\rangle$ in the inertial–convective subrange exists and was given by Yaglom (1949):

$$\langle(\Delta u(r))(\Delta\theta(r))^2\rangle = -\tfrac{4}{3}\epsilon_\theta r, \tag{19}$$

where, here (and here only) because of convention, ϵ_θ is defined as half the value we previously used. We plot this combined third-order structure function normalized by $-\epsilon_\theta r$ so that it should be 4/3 in the inertial–convective subrange. For the lowest Reynolds numbers, the compensated structure function departs from the 4/3 law, presumably retarded by the velocity field which evolves at a slower pace than the temperature field with Reynolds number.

4.4. *The fine-scale structure*

In this flow, the velocity field is essentially Gaussian (see M&W) while the temperature field is slightly less so (see figure 2, the p.d.f. of the temperature fluctuations, which is sub-Gaussian). However, at the smallest scales, both fields are highly intermittent and

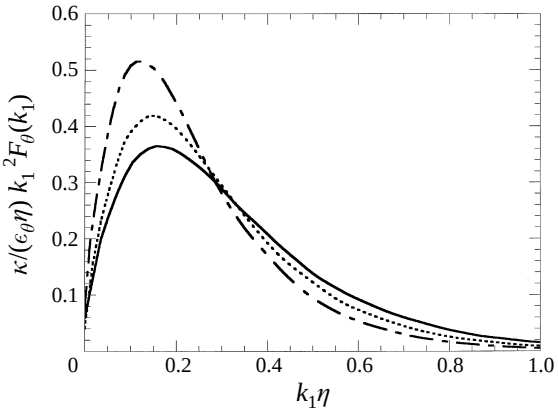

FIGURE 20. Temperature variance 'dissipation' spectra for $R_\lambda = 140$ (horizontal tunnel, synchronous mode; solid line), $R_\lambda = 306$ (horizontal tunnel, random mode; equal length dashed line) and $R_\lambda = 582$ (horizontal tunnel, random mode; unequal length dashed line).

non-Gaussian. In this subsection, we examine the small-scale behaviour of the scalar by observing the derivative statistics and their Reynolds number dependence. In the next subsection, we look at the effects of the intermittency on the inertial subrange.

We begin with a plot of the one-dimensional spectra of temperature multiplied by k_1^2. Figure 20 shows data for $R_\lambda = 140, 306$ and 582. The integral under these non-dimensionalized temperature 'dissipation' spectra (which have been smoothed for clarity) should yield a value of 1/6, since $\epsilon_\theta = 6\kappa\langle(\partial\theta/\partial x)^2\rangle = 6\kappa\int_0^\infty k_1^2 F_\theta(k_1)\mathrm{d}k_1$, which they do to within a few percent. (For consistency, we have used the isotropic estimate of ϵ_θ here, since plotting the one-dimensional spectra of temperature multiplied by k_1^2 is equivalent to plotting the spectrum of $\partial\theta/\partial x$.) As the Reynolds number was increased, the peak of these spectra moved from roughly $k_1\eta \approx 0.16$ to 0.11 and ranged in value from 0.36 to 0.51. The latter is presumably due to the increase in bump size with Reynolds number, as was discussed with respect to figure 6. Our results at the highest Reynolds number agree well with the measurements of Boston & Burling (1972) made in the atmospheric boundary layer: their results (modified by dividing their ordinate by the Prandtl number so as to agree with our non-dimensionalization) peaked at a value of ~ 0.5 for $k_1\eta \approx 0.10$ to 0.15.

Figure 21 shows the p.d.f.s of the longitudinal and transverse temperature derivative for $R_\lambda = 217$ and 731. They strongly depart from the parabolic shape possessed by a Gaussian distribution on a log-linear plot . The skewness of the transverse derivative p.d.f., $S_{\partial\theta/\partial y} \equiv \langle(\partial\theta/\partial y)^3\rangle/\langle(\partial\theta/\partial y)^2\rangle^{3/2}$, is 1.4 for $R_\lambda = 217$ and is 1.2 for $R_\lambda = 731$. The order-one value (as opposed to zero required if small-scale isotropy occurred) of course is evident from the skewness structure function graph (figure 14*a*), which yields the derivative skewness at small spacings.

Tong & Warhaft (1994) found $S_{\partial\theta/\partial y}$ to be 1.8 ± 0.2 and constant over the range $30 < R_\lambda < 130$. Budwig *et al.* (1985) found it to be 1.4 for an isolated measurement in a similar flow. Thoroddsen & Van Atta (1992) measured $S_{\partial\theta/\partial y}$ in stratified grid turbulence. Close to the grid, where buoyancy forces are still negligible, they found $S_{\partial\theta/\partial y}$ to be approximately 1.2. The numerical experiments of Holzer & Siggia (1994) and of Pumir (1994) were broadly consistent with those of Tong and Warhaft. In the present work, we find $S_{\partial\theta/\partial y}$ to vary from 0.6 to 1.6. As was mentioned earlier, the mean temperature gradient, β, decreased with x in our flow, i.e. $\partial\beta/\partial x$ is non-zero.

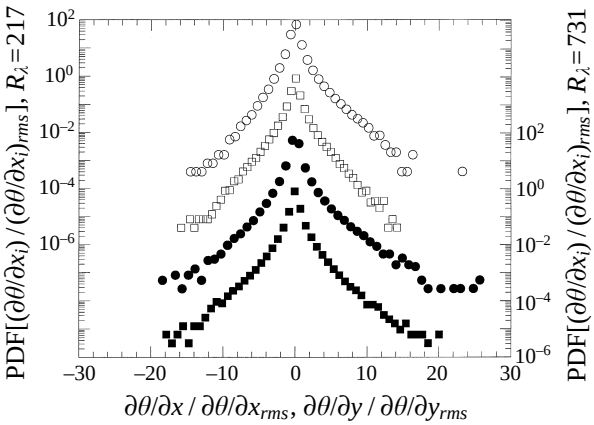

FIGURE 21. Probability density functions (p.d.f.s) of the temperature derivatives normalized by their r.m.s. value. Open symbols are for $R_\lambda = 217$ (horizontal tunnel, synchronous mode) and solid symbols are for $R_\lambda = 731$ (horizontal tunnel, random mode). Squares are the p.d.f.s of $\partial\theta/\partial x$ (i.e. $x_i = x_1$) and circles are the p.d.f.s of $\partial\theta/\partial y$ (i.e. $x_i = x_2$) which have been shifted up by two decades for clarity. For $R_\lambda = 217$, $S_{\partial\theta/\partial x} = 0.028$, $K_{\partial\theta/\partial x} = 18.4$, $S_{\partial\theta/\partial y} = 1.4$ and $K_{\partial\theta/\partial y} = 23.0$. For $R_\lambda = 731$, $S_{\partial\theta/\partial x} = 0.064$, $K_{\partial\theta/\partial x} = 28.0$, $S_{\partial\theta/\partial y} = 1.2$ and $K_{\partial\theta/\partial y} = 34.2$.

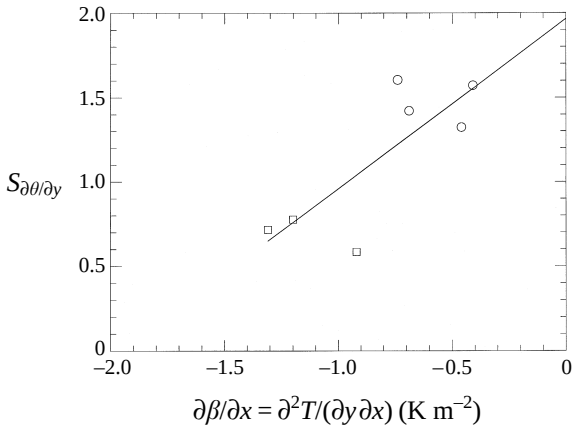

FIGURE 22. The transverse temperature derivative skewness, $S_{\partial\theta/\partial y}$, as a function of the downstream decay of the temperature gradient, $\partial\beta/\partial x$. Circles are for the synchronous mode and squares are for the random mode.

We believe this reduces $S_{\partial\theta/\partial y}$ in some manner by an 'attenuation' of the ramp-cliff structures. We base our arguments on the fact that $S_{\partial\theta/\partial y}$ was always lower when the grid was operated in the random mode than when it was operated in the synchronous mode and that $\partial\beta/\partial x$ was always much larger in the random mode. This can be seen in figure 22 which plots $S_{\partial\theta/\partial y}$ as a function of $\partial\beta/\partial x$ for data recorded at $x/M = 62$ and 68. (Data in our vertical tunnel were generally recorded at $x/M = 68$, while data in our horizontal tunnel were generally recorded at $x/M = 62$; see table 1.) We believe the decay of the gradient results from boundary effects (discussed in §3) which are worsened in the random mode due to its larger integral scale. A best-fit line to the data in figure 22 is shown. Extrapolation of this curve to $\partial\beta/\partial x = 0$ suggests that the value of $S_{\partial\theta/\partial y}$ for a constant gradient would be 1.97, which agrees well with the experiments of Tong & Warhaft (1994) where the temperature gradient did not

evolve. This behaviour is qualitatively similar to the dependence of the turbulent heat flux correlation coefficient on $\partial\beta/\partial x$, as discussed in §4.2.

All our transverse temperature derivative skewness data are plotted in figure 23(*a*). Apart from the data recorded far downstream ($x/M > 60$) with the grid operating in the random mode (circles – where we believe our results are affected by the mean temperature gradient evolution), our results support the notion of Reynolds number independence of the derivative skewness. In addition to Tong & Warhaft (1994), whose data are shown in this figure, Sreenivasan (1991)† observes an approximate Reynolds number independence of the derivative skewness for the scalar.

In figure 23(*b*), we show the Reynolds number dependence of the kurtosis of the longitudinal and transverse temperature fluctuation derivatives. Included in this plot are the data of Tong & Warhaft (1994). Their trend is continued, showing the increasing importance of internal intermittency of the scalar as the Reynolds number rises. The claim that the scalar is much more intermittent than the velocity is supported by a comparison of this figure with the analogous figure for the kurtosis of the velocity derivatives from M&W, figure 21(*b*), which shows that at the same Reynolds number, the kurtosis of the (longitudinal or transverse) derivative of the scalar fluctuations is roughly double the kurtosis of the longitudinal derivative of the (longitudinal or transverse) velocity fluctuations. This notion will be supported upon an examination of the p.d.f.s of velocity and temperature differences in the next subsection. Note that the fourth-order transverse derivative statistics appear to be less affected by the decay of the gradient than are the third-order ones. Recently, Kerstein (1996) has presented a model (based on the idea that intermittency properties in turbulence are determined by a direct coupling between the largest and inertial range scales) for the (normalized) moments of temperature derivative. He predicts that the kurtosis of the scalar derivative should vary as $R_\ell^{1/4}$ which corresponds to an $R_\lambda^{1/2}$ dependence. This is not inconsistent with our results and also agrees well with the data compiled by Antonia & Chambers (1980) for shear flows as well as a ramp-cliff model proposed by C. Tong (private communication).

Figure 23(*c*) shows the hyperskewness (the normalized fifth moment) of the transverse temperature derivative ($\langle(\partial\theta/\partial y)^5\rangle/\langle(\partial\theta/\partial y)^2\rangle^{5/2}$) as a function of the Reynolds number. Its value is on the order of 10^2; isotropy requires it to be zero. As with the skewness, its value appears to be affected by the decay of the temperature gradient. This is most strongly exhibited by the measurements made in the random mode far downstream (circles). Apart from these points, it seems to be approximately constant (or possibly exhibiting a weak upward trend).

4.5. *The conditional statistics*

At a large enough Reynolds number, the effect of internal intermittency will not be solely confined to the dissipation scales: it will be evident in the inertial–convective subrange statistics. For the velocity field, M&W found that this occurs for $R_\lambda > 200$ and is a strong function of R_λ. Here, we examine the Reynolds number dependence of the inertial-range intermittency behaviour of the scalar field.

As in, for example, Zhu, Antonia & Hosokawa (1995) and Stolovitzky, Kailasnath & Sreenivasan (1995), we consider statistics of the difference of temperature fluctuations

$$\Delta\theta(r) = \theta(x+r) - \theta(x), \tag{20}$$

† Sreenivasan's (1991) observation is primarily based on measurements in shear flows where the constant value of the derivative skewness is roughly 0.8. The derivative skewness in shear flows has been found to be roughly half the value in isotropic grid turbulence.

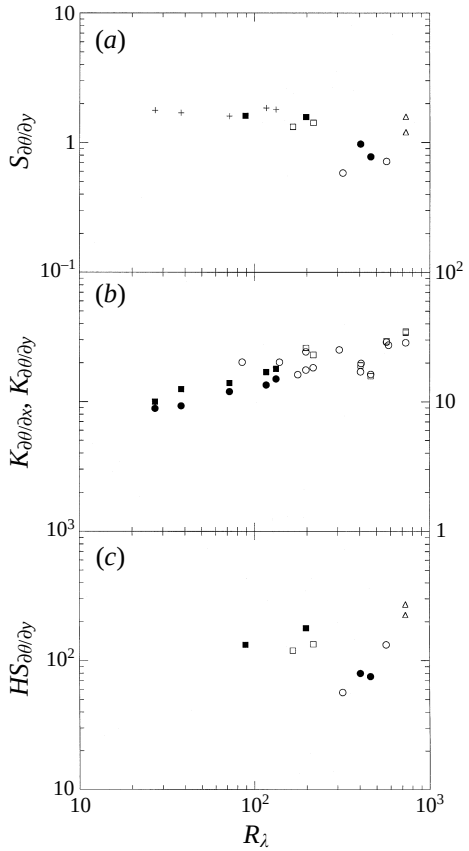

FIGURE 23. (*a*) The transverse temperature derivative skewness, $S_{\partial\theta/\partial y}$, as a function of R_λ. Solid symbols represent data measured in the vertical tunnel. Open symbols represent data measured in the horizontal tunnel. Circles represent data measured with the grid operating in the random mode. Squares represent data measured with the grid operating in the synchronous mode. Plus signs represent the data of Tong & Warhaft (1994) who used a conventional grid. Triangles represent data measured farther upstream ($x/M = 31$). (All other data was measured at $x/M > 60$.) We note that $\partial\beta/\partial x$ was not measured for the data at $R_\lambda \approx 730$. (*b*) The kurtosis of the temperature derivative as a function of R_λ. Circles represent the longitudinal derivative kurtosis. Squares represent the transverse derivative kurtosis. Solid symbols represent the data of Tong & Warhaft (1994) who used a conventional grid. Open symbols represent the present work. (*c*) The transverse temperature derivative hyperskewness, $HS_{\partial\theta/\partial y}$, as a function of R_λ. Same symbols as figure (*a*).

where r is an inertial-range distance. To appropriately compare difference statistics for data at different Reynolds numbers (and therefore with different inertial range widths due to their dilation with Reynolds number), we pick separations, r, such that they occur in the same relative position on the spectrum at any Reynolds number. This is done by considering two values of r, which we call r_a and r_b, where the former corresponds to the middle of the inertial range plotted in linear coordinates and the latter corresponds to the middle of the inertial range plotted in logarithmic coordinates. This method is explained in detail in M&W.

The normalized p.d.f.s of Δu and $\Delta\theta$ for the separation r_a (for $R_\lambda = 140$ and 582) are shown in figure 24. For the same separation and Reynolds number, the p.d.f. of the temperature difference is much less Gaussian than that of the velocity difference. At the low Reynolds number, the velocity difference p.d.f. is close to Gaussian, while

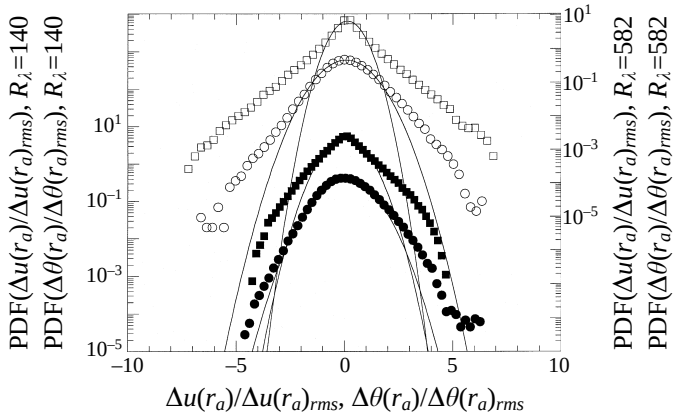

FIGURE 24. Probability density functions (p.d.f.s) of the temperature differences (squares) and longitudinal velocity (u) differences (circles) for the r_a spacing normalized by their r.m.s. value. Solid symbols (lower curves, left ordinate) are for $R_\lambda = 140$ (horizontal tunnel, synchronous mode) where $K_{\Delta u(r_a)} = 3.61$ and $K_{\Delta\theta(r_a)} = 4.26$. Open symbols (upper curves, right ordinate) are for $R_\lambda = 582$ (horizontal tunnel, random mode) where $K_{\Delta u(r_a)} = 4.09$ and $K_{\Delta\theta(r_a)} = 7.14$. Temperature difference p.d.f.s have been shifted up one decade. Lines are the best-fit Gaussians.

the temperature difference p.d.f. is certainly super-Gaussian. This implies that the effects of internal intermittency in the scalar field are exhibited at lower Reynolds numbers than for the velocity field. Using the r_b separation (not shown) produced the same results, though all p.d.f.s were less Gaussian since the effect of intermittency increases in significance as the scale size is reduced.

The refined similarity hypothesis (RSH) for the passive scalar (put forth by Korchashkin 1970 and Van Atta 1971 and further discussed by, for example, Antonia & Van Atta 1975, Meneveau *et al.* 1990, Stolovitzky *et al.* 1995 and Zhu *et al.* 1995) states that in the limit of infinite Reynolds number for a fluid of unity Prandtl number, the temperature difference $\Delta\theta(r)$ (where r is an inertial-range length) is related to the separation, r, the dissipation rate of turbulent kinetic energy averaged over a sphere of radius r, ϵ_r, and the 'dissipation' rate of turbulent temperature variance averaged over a sphere of radius r, ϵ_{θ_r} by

$$\Delta\theta(r) = V_\theta r^{1/3} {\epsilon_r}^{-1/6} {\epsilon_{\theta_r}}^{1/2} \tag{21}$$

where V_θ is a non-dimensional stochastic variable. As in M&W, we examine the dependence among these variables with the use of conditional averaging. In figure 25(a), we have plotted $({r_b}^{1/3}\epsilon_{r_b}^{11\,-1/6}\epsilon_{\theta_{r_b}}{}^{1/2})$ and $({r_b}^{1/3}\epsilon_{r_b}^{21\,-1/6}\epsilon_{\theta_{r_b}}{}^{1/2})$ conditioned on $\Delta\theta(r_b)$. Here $\epsilon_{r_b}^{11}(\equiv 15\nu U_\circ^{-2}\langle(\partial u/\partial t)^2\rangle)$, $\epsilon_{r_b}^{21}(\equiv (7.5\nu U_\circ^{-2}\langle(\partial v/\partial t)^2\rangle)$ and $\epsilon_{\theta_{r_b}}(\equiv 6\kappa U_\circ^{-2}\langle(\partial\theta/\partial t)^2\rangle)$ are (one-dimensional surrogates for the total dissipations of turbulent kinetic energy and temperature variance) determined over a record of length r_b, from which we also obtained $\Delta\theta(r_b)$ from the temperature difference between the start and end of the record. The data have been normalized by $({r_b}^{1/3}\langle\epsilon^{11}\rangle^{-1/6}\langle\epsilon_\theta\rangle^{1/2})$ or $({r_b}^{1/3}\langle\epsilon^{21}\rangle^{-1/6}\langle\epsilon_\theta\rangle^{1/2})$ and have been plotted as a function of $\Delta\theta(r_b)$ normalized by its r.m.s. value. The data are plotted for $R_\lambda = 85$ and 582. The strong correlation between large values of the product of the (surrogate of the volume-averaged) dissipations and large temperature differences is obvious from the strong V shape of the curves, as is the independence of this result with respect to the Reynolds number. This is in sharp contrast with the velocity field, which showed no dependence at the lowest Reynolds numbers but then

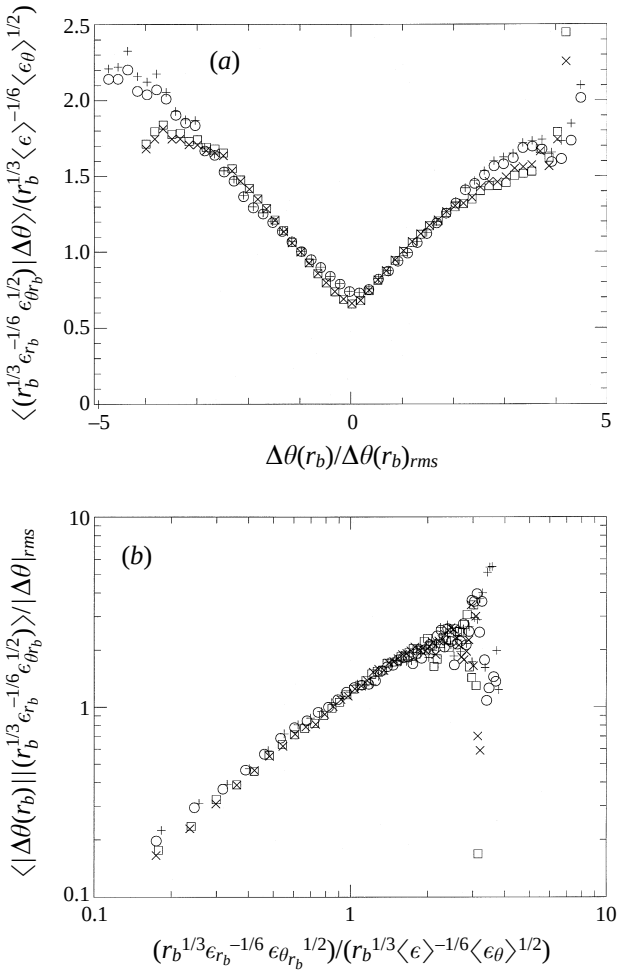

FIGURE 25. (*a*) The expected value of $(r_b^{1/3}\epsilon_{r_b}^{-1/6}\epsilon_{\theta r_b}^{1/2})$ conditioned on $\Delta\theta(r_b)$ and the (*b*) expected value of $|\Delta\theta(r_b)|$ conditioned on $(r_b^{1/3}\epsilon_{r_b}^{-1/6}\epsilon_{\theta r_b}^{1/2})$. Normalizations are by the non-volume averaged dissipations and the r.m.s. of the temperature differences. Circles and plus signs are for $R_\lambda = 582$ (horizontal tunnel, random mode). Squares and crosses are for $R_\lambda = 85$ (vertical tunnel, synchronous mode). Circles and squares are for $\epsilon_{r_b} = \epsilon_{r_b}^{11}$. Crosses and pluses are for $\epsilon_{r_b} = \epsilon_{r_b}^{21}$.

showed a significant dependence (between the analogous quantities under consideration for the velocity field – see M&W figure 26) when the Reynolds number was increased. This calculation was also performed for the r_a spacing which yielded the same result. It should also be noted that whether the grid was operated in the random or synchronous modes, or whether a static grid was used, the results were consistent.

The 'reverse' conditional expectation is shown in figure 25(*b*) (for the same Reynolds numbers as in figure 25*a*) where we have plotted $|\Delta\theta(r_b)|$ (normalized by its r.m.s. value) conditioned on $(r_b{}^{1/3}\epsilon_{r_b}^{11\,-1/6}\epsilon_{\theta_{r_b}}{}^{1/2})$ and $(r_b{}^{1/3}\epsilon_{r_b}^{21\,-1/6}\epsilon_{\theta_{r_b}}{}^{1/2})$, normalized using average dissipations. Were the proposed dependence to exist between the quantities under consideration, the result would be a power law of exponent +1. As can be seen, this is the case, indicating a strong dependence. The correlation coefficients between the (absolute value of the) temperature difference and the product of the (surro-

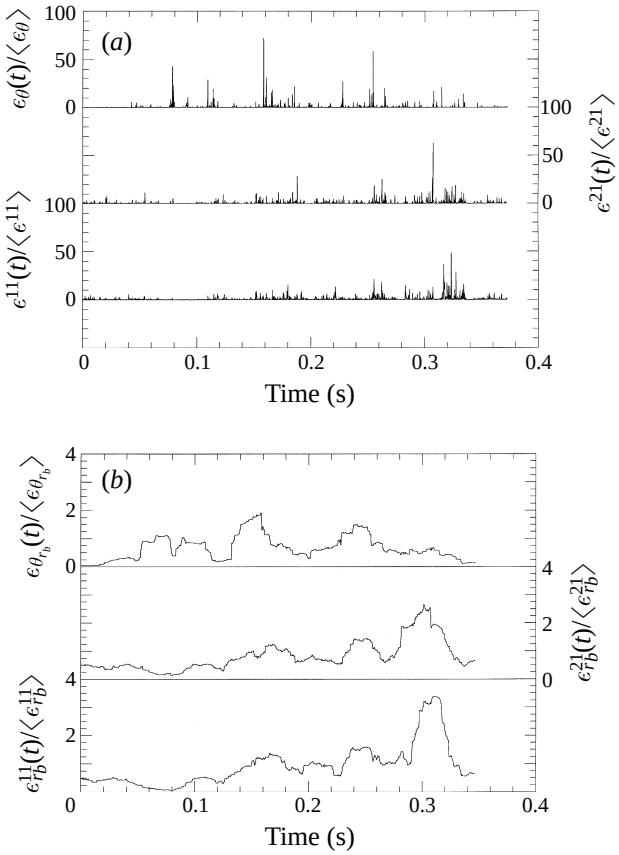

FIGURE 26. Time series of (*a*) ϵ^{11}, ϵ^{21} and ϵ_θ (normalized by their average value), and (*b*) $\epsilon_{r_b}^{11}, \epsilon_{r_b}^{21}$ and $\epsilon_{\theta_{r_b}}$ (normalized by their average value) for $R_\lambda = 582$ (horizontal tunnel, random mode).

gates of the volume-averaged) dissipations for $R_\lambda = 85$ are $\rho_{|\Delta\theta(r_b)|,(r_b{}^{1/3}\epsilon_{r_b}^{11\,-1/6}\epsilon_{\theta_{r_b}}{}^{1/2})} = \rho_{|\Delta\theta(r_b)|,(r_b{}^{1/3}\epsilon_{r_b}^{21\,-1/6}\epsilon_{\theta_{r_b}}{}^{1/2})} = 0.51$, and are $\rho_{|\Delta\theta(r_b)|,(r_b{}^{1/3}\epsilon_{r_b}^{11\,-1/6}\epsilon_{\theta_{r_b}}{}^{1/2})} = \rho_{|\Delta\theta(r_b)|,(r_b{}^{1/3}\epsilon_{r_b}^{21\,-1/6}\epsilon_{\theta_{r_b}}{}^{1/2})} = 0.45$ for $R_\lambda = 582$. We have not found any such calculations (at the first order) for comparison. At the second order, Zhu *et al.* (1995) show the proposed dependence for measurements made in a circular jet at $R_\lambda = 250$ and in the atmospheric surface layer at an $R_\lambda \approx 7200$ in their figure 3(*b*). This result is entirely consistent with ours.

We now investigate the source the above-displayed dependence. In particular, we examine whether the dependence of the temperature difference on the product of the dissipations arises from a dependence on the dissipation of turbulent kinetic energy, the 'dissipation' of scalar variance, or both. This will be performed by calculations similar to those in figure 25, except that we shall only use one dissipation, rather than their product, in the conditional expectations. But we begin by examining the dissipation time series.

Figure 26(*a*) shows a time series of our three measured dissipations – similar to figure 1 from Meneveau *et al.* (1990) – at $R_\lambda = 582$. Visual inspection shows a strong correlation between the two components of the dissipation of turbulent kinetic energy. If the correlation between either of these components and the component of the scalar 'dissipation' exists, it is by no means as strong. In fact, for this flow, the correlation coefficients were $\rho_{\epsilon^{11},\epsilon^{21}} = 0.27, \rho_{\epsilon^{11},\epsilon_\theta} = 0.092$ and $\rho_{\epsilon^{21},\epsilon_\theta} = 0.037$. But, to formally

examine the relationships involved in figure 25, we should compare the (surrogates of the) volume-averaged dissipations. Time series of the three averaged dissipations are shown in figure 26(*b*) where the averaging is performed over an interval of length r_b. We can see from the figure that the correlation between the averaged dissipations is extremely high for the two kinetic energy dissipations, but there is little correlation between those dissipations and that of the scalar variance 'dissipation'. The correlation coefficients are $\rho_{\epsilon_{r_b}^{11},\epsilon_{r_b}^{21}} = 0.87$, $\rho_{\epsilon_{r_b}^{11},\epsilon_{\theta_{r_b}}} = 0.13$ and $\rho_{\epsilon_{r_b}^{21},\epsilon_{\theta_{r_b}}} = 0.087$. The correlation coefficients for the smaller separation, r_a, were found to be $\rho_{\epsilon_{r_a}^{11},\epsilon_{r_a}^{21}} = 0.74$, $\rho_{\epsilon_{r_a}^{11},\epsilon_{\theta_{r_a}}} = 0.14$ and $\rho_{\epsilon_{r_a}^{21},\epsilon_{\theta_{r_a}}} = 0.10$. The results for $\rho_{\epsilon_r^{11},\epsilon_{\theta_r}}$ are in much better agreement with the wake measurements of Meneveau *et al.* (1990) – who find it to be almost constant ($\rho_{\epsilon_r^{11},\epsilon_{\theta_r}} \approx 0.10$) in the range $5 < r/\eta < 200$ – than it is with the results for jet and atmospheric surface layer flows of Zhu *et al.* (1995) and Antonia & Chambers (1980) or the jet flow of Antonia & Van Atta (1975) who all find it to be an increasing function in r/η. However, in the limit of r tending to zero, i.e. no longer volume averaging, our result is consistent with Zhu *et al.* (1995) and Antonia & Chambers (1980) who both find the correlation coefficient to be approximately 0.1 at their smallest spacings. Meneveau *et al.* (1990) attribute the discrepancy at larger r/η to the hot wire influencing the cold wire (and thus artificially increasing the correlation of the dissipations) in a jet flow where the ratio of the fluctuating velocity to the sweeping velocity is not small. This effect is not as severe in the atmospheric surface layer.

For additional insight, instead of conditioning the product of the (surrogate of the volume-averaged) dissipations on the temperature difference (as in figure 25*a*), we condition each dissipation individually on the temperature difference at $R_\lambda = 582$. Figure 27 shows $\epsilon_{r_b}^{11\,-1/6}$ and $\epsilon_{r_b}^{21\,-1/6}$ conditioned on $\Delta\theta(r_b)$ with similar normalizations. The flat nature of this curve implies a lack of dependence between the dissipation of turbulent kinetic energy and temperature differences. Once again, this result was typical for different spacings, Reynolds numbers and modes of operation of the active grid. The expectation (not shown) of $|\Delta\theta(r_b)|$ (normalized by its r.m.s. value) conditioned on $\epsilon_{r_b}^{11\,-1/6}$ and $\epsilon_{r_b}^{21\,-1/6}$ (both normalized) gave the same result. A power law of exponent (or slope on a logarithmic plot) of $+1$ would be expected were the proposed dependence to exist. Indeed, there was no dependence and the correlation coefficients were $\rho_{|\Delta\theta(r_b)|,\epsilon_{r_b}^{11\,-1/6}} = 0.046$ and $\rho_{|\Delta\theta(r_b)|,\epsilon_{r_b}^{21\,-1/6}} = 0.062$.

We also show $\epsilon_{\theta_{r_b}}^{1/2}$ conditioned on $\Delta\theta(r_b)$, with similar normalizations, in the left-hand insert of figure 27 at $R_\lambda = 85$ and 582. The strong dependence associating large values of the (surrogate of the volume-averaged) scalar dissipation with large temperature differences is obvious from the strong V shape of the plot similar to that of figure 25(*a*). This dependence exists from our lowest to highest Reynolds number, as well as for various spacings and for both modes of operation of the active grid. The expectation of $|\Delta\theta(r_b)|$ conditioned on $\epsilon_{\theta_{r_b}}^{1/2}$ is shown in the right-hand insert of figure 27, giving the same result – a strong dependence between the temperature difference and its dissipation. The power law of slope 1 is observed and the correlation coefficient†, $\rho_{|\Delta\theta(r_b)|,\epsilon_{\theta_{r_b}}^{1/2}} = 0.50$ for $R_\lambda = 85$ and 0.43 for $R_\lambda = 582$. These values are

† It should be noted that when the scalar 'dissipation' was calculated from $\epsilon_{\theta_{r_b}} \equiv 6\kappa\langle(\partial\theta/\partial y)^2\rangle_{r_b}$ (not shown), the same results were also observed (Mydlarski & Warhaft 1995). This indicates that the strong dependence is dynamic rather than kinematic. Comparison should be made with the (small) kinematic dependencies of velocity differences on the dissipation of turbulent kinetic energy observed in M&W.

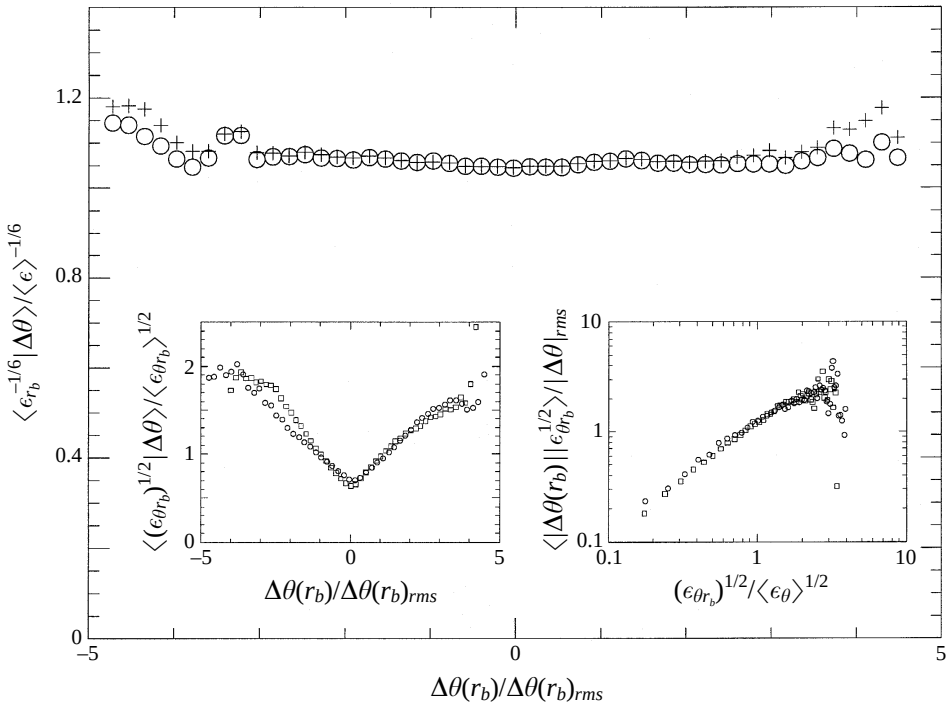

FIGURE 27. The expected value of $\epsilon_{r_b}^{-1/6}$ conditioned on $\Delta\theta(r_b)$. Normalizations are by the non-volume-averaged dissipation and the r.m.s. of the temperature difference. $R_\lambda = 582$ (horizontal tunnel, random mode). Circles are for $\epsilon_{r_b} = \epsilon_{r_b}^{11}$ and plus signs are for $\epsilon_{r_b} = \epsilon_{r_b}^{21}$. Left-hand insert: The expected value of $\epsilon_{\theta_{r_b}}^{1/2}$ conditioned on $\Delta\theta(r_b)$. Right-hand insert: The expected value of $|\Delta\theta(r_b)|$ conditioned on $\epsilon_{\theta_{r_b}}^{1/2}$. Normalizations are by the non-volume-averaged dissipations and the r.m.s. of the temperature differences. For the inserts, circles are for $R_\lambda = 582$ (horizontal tunnel, random mode). Squares are for $R_\lambda = 85$ (vertical tunnel, synchronous mode).

only marginally smaller than the values (0.51 and 0.45) obtained when performing the 'complete' conditional expectation as given by the RSH for the scalar, indicating that the strong correlation when the 'complete' RSH is tested is primarily obtained from strong correlation between the temperature differences and the scalar 'dissipation'. That is, the contribution to the 'complete' RSH from the velocity dissipation is small and is therefore dominated by the more intermittent scalar field. If the contribution to the conditional expectations from the velocity field were of the same order as that of the scalar field, we would have observed a strong correlation between the volume-averaged dissipations of turbulent kinetic energy and scalar difference in figure 27.

The effect of internal intermittency can be quantified by calculating the intermittency exponents for the velocity and scalar fields, μ and μ_θ, defined here by

$$\rho_{\epsilon\epsilon}(r) = \frac{\langle \epsilon(x)\epsilon(x+r) \rangle}{\langle \epsilon^2 \rangle} \propto r^{-\mu} \tag{22}$$

and

$$\rho_{\epsilon_\theta\epsilon_\theta}(r) = \frac{\langle \epsilon_\theta(x)\epsilon_\theta(x+r) \rangle}{\langle \epsilon_\theta^2 \rangle} \propto r^{-\mu_\theta}, \tag{23}$$

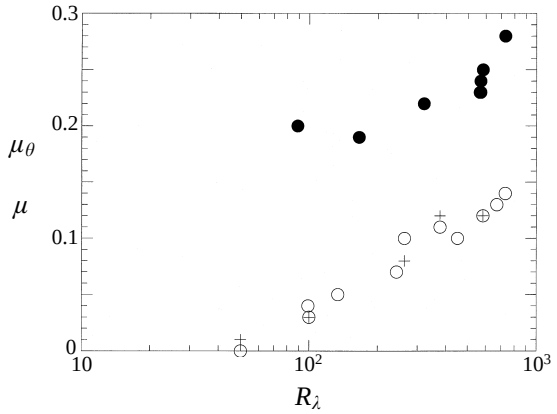

FIGURE 28. The velocity and scalar intermittency exponents, μ and μ_θ respectively, as a function of R_λ. Open circles are for μ determined from the autocorrelation of ϵ^{11}. Plus signs are for μ determined from the autocorrelation of ϵ^{21}. Solid circles are for μ_θ (determined from the autocorrelation of ϵ_θ).

where r is an inertial–convective subrange distance (see for example Chambers & Antonia 1984 or Sreenivasan & Kailasnath, 1993). Typical curves for $\rho_{\epsilon\epsilon}(r)$ are shown in M&W figure 30(a). Plots of $\rho_{\epsilon_\theta\epsilon_\theta}(r)$ are quite similar. The intermittency exponent was determined by compensating the dissipation auto-correlation by r raised to the exponent μ (or μ_θ) to render the compensated plot horizontal in the inertial range. The internal intermittency exponent for the scalar, μ_θ, is plotted as a function of Reynolds number in figure 28. Also included in this figure are the data of M&W (for the intermittency exponent for the velocity field) as well as some new data at higher Reynolds numbers. The value of μ_θ has already reached its observed value in the atmosphere (at $R_\lambda \sim 10^3 - 10^4$) of $\mu_\theta = 0.25 \pm 0.05$ (Chambers & Antonia 1984 and Antonia *et al.* 1984; Prasad, Meneveau & Sreenivasan (1988) and Sreenivasan *et al.* (1977) estimate $\mu_\theta \approx 0.35$) by an R_λ of less than 100, and appears relatively constant over the whole range of Reynolds numbers. We believe the slight rise at the highest R_λ is primarily scatter, although the range in Reynolds numbers is too small to be able to arrive at a firm conclusion. By contrast, below $R_\lambda \sim 100$, μ is approximately zero and above this Reynolds number it is a strong function of R_λ.

Below $R_\lambda = 100$, where μ was essentially zero, M&W found that the RSH for the velocity field was not observed. This then changed when the Reynolds number was increased and the internal intermittency of the velocity field became significant. Here, we observed the RSH for the passive scalar to hold at all Reynolds numbers. Therefore the fact that we find μ_θ to be significant at all our Reynolds numbers should be no surprise. We also claimed that the contribution to the RSH for the passive scalar came primarily from the correlation between large temperature differences and large values of the volume-averaged scalar 'dissipation'. This may result from the significantly stronger intermittency of the scalar field than the velocity field. It would be of interest to determine whether the contribution to the scalar RSH from the velocity field becomes significant when μ reaches the value of 0.25 ($\approx \mu_\theta$) observed in the atmosphere at very high Reynolds numbers. Perhaps a value of $\mu \sim 0.1$ is sufficient for an interaction to exist between velocity differences and the dissipation rate of turbulent kinetic energy, but is still too low to observe an interaction between temperature differences and the dissipation rate of turbulent kinetic energy.

5. Conclusions

Our study of passive temperature fluctuations in grid turbulence over the Reynolds number range $30 \leqslant R_\lambda \leqslant 731$ has resulted in two broad findings.

First, the statistical nature of the scalar fluctuations at the lowest Reynolds numbers is essentially the same as those at the highest. Thus at all Reynolds numbers the slope of the temperature spectrum is close to 5/3 (figure 7), the conditional statistics are the same (figure 25*a*, *b*) and the intermittency exponent is relatively constant with a value of 0.25 ± 0.05 (figure 28). Of course there is a growth in quantities such as the temperature derivative kurtosis (figure 23*b*) and the width of the scaling region in the temperature spectrum, but the essential point is that there appears to be no qualitative change in the nature of the structure of the thermal fluctuations with Péclet number. This is in marked contrast to that of the velocity field in the same flow. Mydlarski & Warhaft (1996) found a qualitative change in the velocity field over the same Reynolds number range, changing from weak turbulence, with no inertial subrange (and with $\mu = 0$), to strong turbulence, with a fully developed inertial subrange, at around $R_\lambda \sim 200$. It is evident, then, that the temperature field displays 'high Reynolds and Péclet number' behaviour even when the turbulence itself is at a decidedly low Reynolds number. Holzer & Siggia (1994) and Cao & Chen (1996), in numerical experiments, have pointed out that the scalar and velocity fields have different morphology in simple flows. For example, Holzer and Siggia (1994) find significant kurtosis for the scalar field within a purely Gaussian velocity field.

Second, our results show that the scalar field is anisotropic, both in the inertial subrange and at the dissipation scales. This too is independent of Péclet number. Thus, along the mean gradient, the temperature derivative skewness and hyperskewness are of order 1 and 100 respectively (figures 23*a* and 23*c*) and there are well developed third- and fifth-order structure functions (figure 13), showing scaling ranges. Remarkably, the slope of the structure functions increases in a systematic way from second to fifth order, independent of whether they are odd or even.

We have taken particular care to combine the active grid results with the available low-Reynolds-number data from traditional passive grid experiments. The match between the low-Reynolds-number range of the active grid experiments and the passive grid experiments at the same Reynolds and Péclet numbers is excellent, both for the velocity and scalar fields, thus showing that the active grid behaves in the manner for which it was designed, i.e. to extend the Reynolds number range of grid turbulence to values previously only accessible in geophysical flows. By achieving a broad range of Reynolds numbers in a single simple flow, our experiments show clear trends in the various statistical properties and thereby imply the turbulence behaviour in the high-Reynolds- and Péclet-number limit.

Our results are consistent in some ways with scalars in shear flows, but in other ways, they are quite different. Antonia & Van Atta (1978) observed a similar behaviour to us for the odd- and even-order structure functions in shear flows. On the other hand in shear flows, the scalar field does not achieve a 5/3 spectral slope until very high Reynolds numbers (approximately $R_\lambda \sim 2000$, see Sreenivasan 1991). This is in strong contrast to our observations in grid turbulence. Unfortunately, there do not appear to be any passive scalar shear flow experiments in which the Reynolds number is varied in a systematic way. So we do not know, for example, how μ_θ varies with Reynolds number in shear flows.

Our observations suggest that the Kolmogorov–Obukhov–Corrsin phenomenology for scalars in turbulence and the more recent modifications that include the effects of

internal intermittency (see for example Sreenivasan & Antonia 1997 for a review) are fundamentally deficient: the basic postulate of local isotropy does not occur even at high Péclet number, and moreover, the requirement of high Pe (and significant separation of scales) does not have to be met in order to observe a 5/3 spectrum. Indeed, our experiments suggest that, at least for decaying isotropic turbulence, a successful theory for the behaviour of the scalar will not need to be constructed in terms of an infinite-Reynolds- or Péclet-number limit, as it must be for the velocity field.

It is important to point out that although the passive scalar field is mixed and advected by the decaying velocity field, unlike the velocity, it has a production mechanism because of its mean gradient. Thus it might be inferred that the differences between the scalar and velocity fields may be a result of the different boundary conditions. However in Jayesh *et al.* (1994), as well as in other grid turbulence experiments (Sreenivasan 1996), measurements were done for a decaying scalar field (with no mean gradient). In these experiments too, a 5/3 spectrum was observed at low Reynolds number (however, μ_θ was not determined). So there is evidence to suggest that our conclusion (that the scalar spectrum is close to 5/3 and the RSH holds at all R_λ) does not depend on the scalar boundary conditions, as long as the requirement of an isotropic velocity field is met. (Whether it must be decaying as well, is unclear.)

Finally, with regard to the anisotropy issue, Pumir & Shraiman (1995) and Pumir (1996) have found that there is an analogy between the scalar field with a mean scalar gradient and the velocity field with a mean velocity gradient. They show, using numerical simulations, that there exists significant velocity derivative skewness along the velocity gradient, just as for the scalar derivative skewness along its own gradient. Earlier experiments had also reported non-zero skewness for this quantity (e.g. Tavoularis & Corrsin 1981*a*). Experiments in our own laboratory in a flow with linear shear (Garg & Warhaft 1998) show not only skewness of order 1 for the velocity derivative along the gradient, but also fully developed third- and fifth-order structure functions, making the analogy even stronger. Clearly, our understanding of the small-scale structure of both the scalar and velocity fields is far from complete. Most pertinently, the notion of local isotropy, the cornerstone of modern phenomenology, needs careful re-evaluation.

As always, we thank Mr E. P. Jordan for his most helpful assistance. We also thank Dr C. Tong who carried out some preliminary experiments and Professor E. D. Siggia for beneficial discussions. The work was supported by the Department of Energy (Basic Energy Sciences).

REFERENCES

Antonia, R. A. & Chambers, A. J. 1980 On the correlation between turbulent velocity and temperature derivatives in the atmospheric surface layer. *Boundary-Layer Met.* **18**, 399–410.

Antonia, R. A., Chambers, A. J., Friehe, C. A. & Van Atta, C. W. 1979 Temperature ramps in the atmospheric surface layer. *J. Atmos. Sci.* **36**, 99–108.

Antonia, R. A., Hopfinger, E. J., Gagne, Y. & Anselmet, F. 1984 Temperature structure functions in turbulent shear flows. *Phys. Rev.* A **30**, 2704–2707.

Antonia, R. A. & Van Atta, C. W. 1975 On the correlation between temperature and velocity dissipation fields in a heated turbulent jet. *J. Fluid Mech.* **67**, 273–288.

Antonia, R. A. & Van Atta, C. W. 1978 Structure functions of temperature fluctuations in turbulent shear flows. *J. Fluid Mech.* **84**, 561–580.

Bendat, J. S. & Piersol, A. G. 1986 *Random Data: Analysis and Measurement Procedures.* Wiley.

Boston, N. E. J. & Burling, R. W. 1972 An investigation of high-wavenumber temperature and velocity spectra in air. *J. Fluid Mech.* **55**, 473–492.

Browne, L. W. B. & Antonia, R. A. 1987 The effect of wire length on temperature statistics in a turbulent wake. *Exps. Fluids* **5**, 426–428.

Browne, L. W. B., Antonia, R. A. & Chua, L. P. 1989 Calibration of X-probes for turbulent flow measurements. *Exps. Fluids* **7**, 201–208.

Budwig, R., Tavoularis, S. & Corrsin, S. 1985 Temperature fluctuations and heat flux in grid generated isotropic turbulence with streamwise and transverse mean-temperature gradients. *J. Fluid Mech.* **153**, 441–460.

Cao, N. & Chen, S. 1996 Numerical studies of three-dimensional passive scalar turbulence. *Bull. Am. Phys. Soc.* **41**, 1755. Abstract only.

Chambers, A. J. & Antonia, R. A. 1984 Atmospheric estimates of power law exponents μ and μ_θ. *Boundary-Layer Met.* **28**, 343–352.

Champagne, F. H., Friehe, C. A., LaRue, J. C. & Wyngaard, J. C. 1977 Flux measurements, flux estimation techniques, and fine-scale turbulence measurements in the unstable surface layer over land. *J. Atmos. Sci.* **34**, 515–530.

Comte-Bellot, G. & Corrsin, S. 1966 The use of a contraction to improve the isotropy of grid-generated turbulence. *J. Fluid Mech.* **25**, 657–682.

Corrsin, S. 1951 On the spectrum of isotropic temperature fluctuations in isotropic turbulence. *J. Appl. Phys.* **22**, 469–473.

Corrsin, S. 1952 Heat transfer in isotropic turbulence. *J. Appl. Phys.*, **23**, 113–118.

Frisch, U. 1995 *Turbulence: the Legacy of A. N. Kolmogorov*. Cambridge University Press.

Garg, S. & Warhaft, Z. 1998 On small scale statistics in a simple shear flow. *Phys. Fluids* (In press).

Gibson, C. H., Friehe, C. A. & McConnell, S. O. 1977 Skewness of temperature derivatives in turbulent shear flows. *Phys. Fluids Supp.* **20**, s156–s167.

Haughdal, J. & Lienhard, V. H. 1988 A low cost high performance cold wire bridge. *J. Phys.* E **21**, 167–170.

Hill, R. J. 1978 Models of the scalar spectrum for turbulent advection. *J. Fluid Mech.* **88**, 541–562.

Hinze, J. O. 1975 *Turbulence*. McGraw Hill.

Holzer, M. & Siggia E. D. 1994 Turbulent mixing of a passive scalar. *Phys. Fluids* **6**, 1820–1837.

Jayesh, Tong, C. & Warhaft, Z. 1994 On temperature spectra in grid turbulence. *Phys. Fluids* **6**, 306–312.

Jayesh & Warhaft, Z. 1992 Probability distribution, conditional dissipation, and transport of passive temperature fluctuations in grid generated turbulence. *Phys. Fluids* A **4**, 2292–2307.

Jayesh, Yoon, K. & Warhaft, Z. 1991 Turbulent mixing and transport in a thermally stratified interfacial layer in decaying grid turbulence. *Phys. Fluids* A **3**, 1143–1155.

Kerstein, A. R. 1996 Intermittency interpretation of persistent small scale anisotropy in turbulence. *Phys. Rev.* E **53**, 5569–5571.

Kolmogorov, A. N. 1941*a* The local structure of turbulence in incompressible viscous fluid for very large Reynolds numbers. *Dokl. Akad. Nauk. SSSR* **30**, 301–305.

Kolmogorov, A. N. 1941*b* Dissipation of energy in locally isotropic turbulence. *Dokl. Akad. Nauk. SSSR* **32**, 16–18.

Korchashkin, N. N. 1970 The effect of fluctuations of energy dissipation and temperature dissipation on locally isotropic turbulent fields. *Izv. Atmos. Oceanic Phys.* **6**, 947–949.

LaRue, J. C., Deaton, T. & Gibson, C. H. 1975 Measurement of high-frequency turbulent temperature. *Rev. Sci. Instrum.* **46**, 757–764.

Lienhard, J. H. 1988 The decay of turbulence in thermally stratified flow. PhD dissertation, University of California at San Diego.

Lohse, D. & Müller-Groeling, A. 1996 Anisotropy and scaling corrections in turbulence. *Phys. Rev.* E **54**, 395–405.

Lumley, J. L. 1967 Similarity and the turbulent energy spectrum. *Phys. Fluids* **10**, 855–858.

Ma, B. & Warhaft, Z. 1986 Some aspects of the thermal mixing layer in grid turbulence. *Phys. Fluids* **29**, 3114–3120.

Makita, H. 1991 Realization of a large-scale turbulence field in a small wind tunnel. *Fluid Dyn. Res.* **8**, 53–64.

Meneveau, C., Sreenivasan, K. R., Kailasnath, P. & Fan, M. S. 1990 Joint multifractal measures: Theory and applications to turbulence. *Phys. Rev.* A **41**, 894–913.

Mestayer, P. G. 1982 Local isotropy and anisotropy in a high-Reynolds-number turbulent boundary layer. *J. Fluid Mech.* **125**, 475–503.

Mestayer, P., Chollet, J. P. & Lesieur, M. 1983 Inertial subrange of velocity and scalar variance spectra in high Reynolds number three-dimensional turbulence. In *Turbulence and Chaotic Phenomena in Fluids* (ed. T. Tatsumi), p. 285. Elsevier.

Mestayer, P. G., Gibson, C. H., Coantic M. F. & Patel, A. S. 1976 Local anisotropy in heated and cooled turbulent boundary layers. *Phys. Fluids* **19**, 1279–1287.

Monin, A. S. & Yaglom, A. M. 1975 *Statistical Fluid Mechanics*, Vol. 2. MIT Press.

Mydlarski, L. & Warhaft, Z. 1995 The temperature spectrum and related statistics in high Reynolds number grid turbulence. *Bull. Am. Phys. Soc.* **40**, 2032. Abstract only.

Mydlarski, L. & Warhaft, Z. 1996 On the onset of high Reynolds number grid generated wind tunnel turbulence. *J. Fluid Mech.* **320**, 331–368.

Mydlarski, L. & Warhaft, Z. 1997 Three-point statistics and the anisotropy of a turbulent passive scalar. In preparation.

Nelkin, M. 1994 Universality and scaling in fully developed turbulence. *Adv. Phys.* **43**, 143–181.

Obukhov, A. M. 1949 Structure of the temperature field in turbulent flows. *Izv. Akad. Nauk. SSSR, Geogr. Geofiz.* **13**, 58–69.

Prasad, R. R., Meneveau, C. & Sreenivasan, K. R. 1988 Multifractal nature of the dissipation field of passive scalars in fully turbulent flow. *Phys. Rev. Lett.* **61**, 74–77.

Pumir, A. 1994 A numerical study of the mixing of a passive scalar in three dimensions in the presence of a mean gradient. *Phys. Fluids* **6**, 2118–2132.

Pumir, A. 1996 Turbulence in homogeneous shear flows. *Phys. Fluids* **8**, 3112–3127.

Pumir, A. & Shraiman, B. I. 1995 Persistent small scale anisotropy in homogeneous shear flows. *Phys. Rev. Lett.* **75**, 3114–3117.

Saddoughi, S. G. & Veeravalli, S. V. 1994 Local isotropy in turbulent boundary layers at high Reynolds number. *J. Fluid Mech.* **268**, 333–372.

Shraiman, B. I. & Siggia, E. D. 1994 Lagrangian path integrals and fluctuations in random flow. *Phys. Rev.* E **49**, 2912–2927.

Sirivat, A. & Warhaft Z. 1983 The effect of a passive cross-stream temperature gradient on the evolution of temperature variance and heat flux in grid turbulence. *J. Fluid Mech.* **128**, 323–346.

Sreenivasan, K. R. 1991 On local isotropy of passive scalars in turbulent shear flows. *Proc. R. Soc. Lond.* A **434**, 165–182.

Sreenivasan, K. R. 1995 On the universality of the Kolmogorov constant. *Phys. Fluids* **7**, 2778–2784.

Sreenivasan, K. R. 1996 The passive scalar spectrum and the Obukhov-Corrsin constant. *Phys. Fluids* **8**, 189–196.

Sreenivasan, K. R. & Antonia, R. A. 1977 Skewness of temperature derivatives in turbulent shear flows. *Phys. Fluids* **20**, 1986–1988.

Sreenivasan, K. R. & Antonia, R. A. 1997 The phenomenology of small-scale turbulence. *Ann. Rev. Fluid Mech.* **29**, 435–472.

Sreenivasan, K. R., Antonia, R. A. & Britz, D. 1979 Local isotropy and large structures in a heated turbulent jet. *J. Fluid Mech.* **94**, 745–775.

Sreenivasan, K. R., Antonia, R. A. & Danh, H. Q. 1977 Temperature dissipation fluctuations in a turbulent boundary layer. *Phys. Fluids* **20**, 1238–1249.

Sreenivasan, K. R. & Kailasnath, P. 1993 An update on the intermittency exponent in turbulence. *Phys. Fluids* **5**, 512–514.

Stolovitzky, G., Kailasnath, P. & Sreenivasan, K. R. 1995 Refined similarity hypotheses for passive scalars mixed by turbulence. *J. Fluid Mech.* **297**, 275–291.

Tatarskii, V. I., Dubovikov, M. M., Praskovsky, A. A. & Karyakin, M. Y. 1992 Temperature fluctuation spectrum in the dissipation range for statistically isotropic turbulent flow. *J. Fluid Mech.* **238**, 683–698.

Tavoularis, S. & Corrsin, S. 1981*a* Experiments in nearly homogeneous turbulent shear flow with a uniform mean temperature gradient. Part 1. *J. Fluid Mech.* **104**, 311–347.

Tavoularis, S. & Corrsin, S. 1981*b* Experiments in nearly homogeneous turbulent shear flow with a uniform mean temperature gradient. Part 2. The fine structure. *J. Fluid Mech.* **104**, 349–367.

THORODDSEN, S. T. & VAN ATTA, C. W. 1992 Exponential tails and skewness of density-gradient probability density functions in stably stratified turbulence. *J. Fluid Mech.* **244**, 547–566.

THORODDSEN, S. T. & VAN ATTA, C. W. 1996 Experiments on density-gradient anisotropies and scalar dissipation of turbulence in a stably stratified fluid. *J. Fluid Mech.* **322**, 383–409.

TONG, C. & WARHAFT, Z. 1994 On passive scalar derivative statistics in grid turbulence. *Phys. Fluids* **6**, 2165–2176.

VAN ATTA, C. W. 1971 Influence of fluctuations in local dissipation rates on turbulent scalar characteristics in the inertial subrange. *Phys. Fluids* **14**, 1803–1804 (see also *Phys. Fluids* **16**, 574).

WILLIAMS, R. M. & PAULSON, C. A. 1977 Microscale temperature and velocity spectra in the atmospheric boundary layer. *J. Fluid Mech.* **83**, 547–567.

WYNGAARD, J.C. 1968 Measurements of small-scale turbulence structure with hot wires. *J. Sci. Instrum.* **1**, 1105–1108.

WYNGAARD, J. C. 1971 Spatial resolution of a resistance wire temperature sensor. *Phys. Fluids* **14**, 2052–2054.

YAGLOM, A. M. 1949 On the local structure of a temperature field in a turbulent flow. *Dokl. Akad. Nauk. SSSR* **69**, 743–746.

YOON, K. & WARHAFT, Z. 1990 The evolution of grid-generated turbulence under conditions of stable thermal stratification. *J. Fluid Mech.* **215**, 601–638.

ZHU, Y., ANTONIA, R. A. & HOSOKAWA, I. 1995 Refined similarity hypotheses for turbulent velocity and temperature fields. *Phys. Fluids* **7**, 1637–1648.